International Journal of Heat and Mass Transfer 213 (2023) 124290

Contents lists available at ScienceDirect

International Journal of Heat and Mass Transfer

journal homepage: www.elsevier.com/locate/hmt

Machine learning-assisted heat transport modelling for full-scale emplacement experiment at Mont Terri underground laboratory

Guang Hu*, Wilfried Pfingsten

Laboratory for Waste Management, Paul Scherrer Institut, 5232 Villigen, Switzerland

ARTICLE INFO

Article history:
Received 14 March 2023
Revised 27 April 2023
Accepted 8 May 2023
Available online 25 May 2023

Keywords:
Heat transport
Neural network
Surrogate model
Parameter uncertainty
Data assessment
FE experiment

ABSTRACT

Machine learning (ML)-assisted modelling of deep geological repositories (DGR) is of emerging interest and can help to improve the safe and reliable operation of DGRs as well as the public acceptance. Here, a concept of ML-assisted physical-based 3D heat transport model for the Full-scale Emplacement (FE) experiment performed at Mont Terri Underground Laboratory (URL), is presented. The FE experiment is a 1:1 scale mock-up of a DGR tunnel where heaters simulate emplaced high level waste. ML is applied to sparse sensor data of the water saturation degree in the granulated bentonite material (GBM) yielding a physically and neural network (NN) based surrogate model for the thermal conductivity of the GBM, needed to calculate the temperature evolution in the FE tunnel near-field. In order to investigate the dominant parameters influencing the temperature evolution in the vicinity of the FE experiment, the results of 32 orthogonal test cases have been analysed systematically.

For the ML predicted water saturation degree, three NN methods are tested. The Elman NN (with a Pearson's r coefficient of 0.9911, a mean squared error (MSE) of 4.62, and mean absolute error (MAE) of 1.44) operates better than the back propagation (BP) and cascade BP (CBP) NN methods. Results of ML-assisted heat transport calculations are validated with the large experimental dataset of 137 $\times$ 10 temperature sensor data points (errors range within 7%). Parameters uncertainty ranges of $\pm$10% for thermal conductivities of the GBM λ_{GBM} and bentonite block λ_{block} are analysed and bands of temperature uncertainties are compared with temperature sensor data, which allows sensor data assessment including identification of the faulty sensor data. The ML-assisted physical modelling framework can be applied to future DGRs.

1. Introduction

Multi-physics and multiscale processes are typically occurring at various subsurface systems including geothermal energy exploitation [1,2], carbon dioxide sequestration [3,4] and radioactive waste disposal [5,6]. Especially, the safe, economical, and reliable long-term operation of the subsurface systems like the deep geological repository (DGR) is a vital issue for permanently isolating the spent fuel/high-level radioactive waste (SF/HLW) from the human environment [7]. SF/HLW produces decay heat for a long time after disposal and the impact of thermal loads on the long-term safety functions of the repository is a key issue [8]. To this end, the Full-scale Emplacement (FE) experiment at the Mont Terri Underground Laboratory (URL) has been set up to obtain a better understanding of the coupled processes at repository scale including their 3D (three-dimensional) modelling. Heat transport is the dominating process within the initial storage phase of SF/HLW, however, it is influenced by coupled processes like water resaturation, bentonite swelling, and other near-field material properties evolving with time. All these parameter evolutions have to be taken into account for the modelling of the temperature evolution [9].

1.1. Heat transport modelling

Various coupled modelling approaches of the DGR near-field include the modelling of the temperature evolution, i.e., the thermal-hydraulic (TH), thermal-hydraulic-chemical (THC), thermal-hydraulic-mechanical (THM), thermal-hydraulic-mechanical-chemical (THMC) modelling [5,10], etc. Many efforts have been proposed to capture all these complex coupled processes. For example, the coupled TH processes are considered to obtain the temperature evolution of the buffer material of the DGR in South Korea [11]; the THM responses of clay based materials (host rock and buffer) exposed to elevated temperatures (>100 °C) for extended durations within the HITEC work package of the

* Corresponding author.
E-mail address: guang.hu@psi.ch (G. Hu).

https://doi.org/10.1016/j.ijheatmasstransfer.2023.124290

Nomenclature

BBW	Bentonite block wall
DDML	Data-driven machine learning
DGR	Deep geological repository
EBS	Engineered barrier system
EDZ	Excavation Damage Zone
EURAD	European Joint Programme on Radioactive Waste Management
FE	Full-scale Emplacement experiment
G1, G2, G3	Sensor G1, G2, G3 in the GBM
GBM	Granulated bentonite material
H1, H2, H3	Heater 1, heater 2, heater 3
H1–1, H1–2	Sensor H1–1, H1–2 near the GBM-heater 1 surface
H2–1, H2–2	Sensor H2–1, H2–2 near the GBM-heater 2 surface
H3–1, H3–2	Sensor H3–1, H3–2 near the GBM-heater 3 surface
HLW	High-level radioactive waste
ILW	Intermediate-level waste
ML	Machine learning
MAE	Mean absolute error
MSE	Mean squared error
NN	Neural network
P_{H1}, P_{H2}, P_{H3}	Heat power of each heater canister
SF	Spent fuel
TH	Thermal-hydraulic
THC	Thermal-hydraulic-chemical
THM	Thermal-hydraulic-mechanical
THMC	Thermal-hydraulic-mechanical-chemical
URL	Underground Laboratory
3D	Three-dimensional
a, b, c	parameters of empirical formula
$a_1 \sim a_5$, $b_1 \sim b_5$	parameters of empirical formula
$C_{P,block}$	Specific heat of the bentonite block
$C_{P,clay}$	Specific heat of the clay
$C_{P,concrete}$	Specific heat of the concrete
$C_{P,EDZ}$	Specific heat of the EDZ
$C_{P,i}$	Specific heat of the medium
L	Distance between heaters centerlines, $L = 7.6$ m
N	Amount of the test dataset
p-value	Probability that the test statistic can take a value greater than or equal to the value of the test statistic, rejection of the null hypothesis if p-value<0.1
Q	Specific heat source
R	Pearson's r coefficient
t	Time
T	Temperature
$T_{C1,t}$	Transient temperature at the position of sensor C1 at $t = 101$ days
$T_{H1-1,t}$	Transient temperature at the position of sensor H1–1 at $t = 101$ days
$T_{H2-1,t}$	Transient temperature at the position of sensor H2–1 at $t = 101$ days
$T_{H3-1,t}$	Transient temperature at the position of sensor H3–1 at $t = 101$ days
$T_{G1,t}$	Transient temperature at the position of sensor G1 at $t = 101$ days
$T_{G3,t}$	Transient temperature at the position of sensor G3 at $t = 101$ days
x, y, z	Coordinates
y_{exp}, $y_{exp,i}$	Experimental dataset, experimental data
y_{pred}, $y_{pred,i}$	Prediction dataset, prediction data
α	Thermal diffusivity
ρ_{block}	Density of the bentonite block
ρ_{clay}	Density of the clay
$\rho_{concrete}$	Density of the concrete
ρ_{EDZ}	Density of the EDZ
ρ_i	Dry density of the medium
$\rho_{GBM,i}$ or ρ_d	Dry density of different sections of the GBM
λ_{block}	Thermal conductivity of the bentonite block
$\lambda_{canister}$	Thermal conductivity of the heater canister
$\lambda_{concrete}$	Thermal conductivity of the concrete
λ_{clay}	Thermal conductivity of the clay
λ_{EDZ}	Thermal conductivity of the EDZ
λ_{GBM}	Thermal conductivity of the GBM, it is a dataset with 10 $\lambda_{GBM,i}$
$\lambda_{GBM,i}$	Thermal conductivity of various parts of the GBM
λ_i	Thermal conductivity of the medium
μ	Mean value
σ	Standard deviation
φ	Centerline location of the heater 1 in the y-axis direction, $\varphi = 35.5$ m

EURAD (European Joint Programme on Radioactive Waste Management) project [12], or an international collaborative research DECOVALEX project working on understanding and modelling of coupled THMC processes in geological systems [13]. In particularly, the HotBENT (High Temperature Effects on Bentonite Buffers) experiment at Grimsel URL aims to evaluate current accepted safety functions by investigating the effects of high temperatures on bentonite-based barriers and their safety functions [14], whereas in [15] the relation of the temperature evolution of the buffer material of the DGR and typical TH processes are described.

Nevertheless, complex physical modelling, such as detailed THMC cannot handle coupled processes efficiently [16]. One reason is the complexity of the multiscale DGR system. Another reason is the nonlinearly coupled equations between multi-physics fields [5]. Recent studies have suggested that the data-driven machine learning (DDML) such as neural network (NN) machine learning (ML) potentially provide an effective method to address such physical and time-consuming incompatibility [5,17]. Therefore, there are efforts, also in other areas [17,18], to make a trade-off between the DDML and physical modelling and combine the ML and physical modelling. This can increase the calculation efficiency and reduce the "black-box" characteristics of pure DDML [16,19,20].

1.2. Neural network machine learning

Application of ML for the disposal of the HLW in the DGR is of interest in the past few years [21–25]. It should be noted that the definitions of the combination of the physical modelling (multi-physics-multiscale calculations for the DGR) with ML and the physical-informed ML are different in principle [17]. The latter so-called physical-informed ML implies that the ML is coupled with physical constraints, theoretical equations and relations to enhance the DDML performance [19,21]. Nevertheless, the combination of the multi-physics-multiscale calculations with ML usually upscale the complex processes from the micro-scale to the macro-scale with the DDML [5,22–24].

Application of the ML in the area of disposal of the HLW in the DGR is of increasing interest in the past few years. Krishnan et al. (2018) [21] combined the physical constraints with an artificial neural network (ANN) to predicate the dissolution rates of

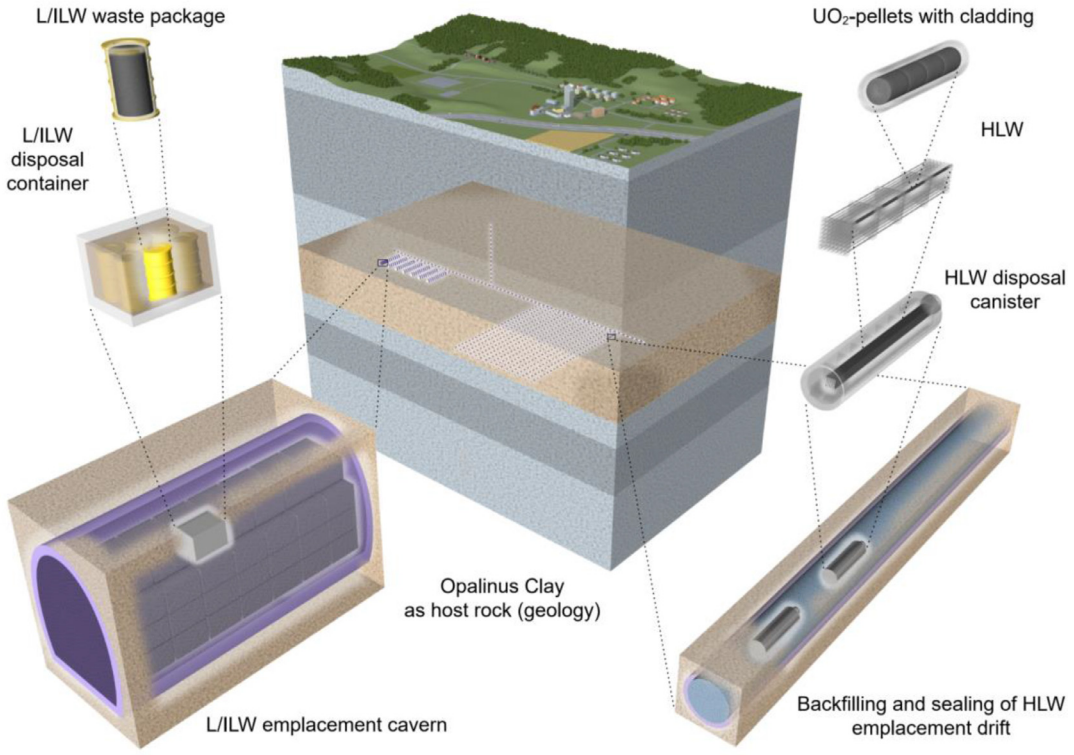

Fig. 1. Safety concept for the HLW and L/ILW repository according to the current disposal project (combined repository) [9]. (For interpretation of the references to color in this figure legend, the reader is referred to the web version of this article.)

silicate glasses in aqueous conditions within the DGR, which belongs to the typical physical-informed ML. Birkholzer et al. (2019) [22] summarized the lessons learned for upscaling THM processes observed in various heater experiments in the DGR. Prasianakis et al. (2020) [5] trained a shallow NN based on the results of microscopic geochemical reactive transport simulations, and integrated it in a Darcy-scale reactive transport code. Tian et al. (2021) [23] proposed a hybrid genetic algorithm (GA)-ANN method with the multi-physics and multiscale calculation. Menke et al. (2021) [24] combined the decision tree from the pore scale porosity to the Darcy-scale permeability with multi-physics and multiscale. Solans et al. (2021) [25] applied a GA-ANN to optimize simultaneously the effective neutron multiplication of the waste canister, to give some examples. Furthermore, the NN based ML technique is a tool, which has been successfully applied to coupled systems [22,23]. However, the ML are applied for either the prediction of individual parameters or upscaling of process. The issue of ML for the multi-physics calculation of a complex underground system is not well-addressed yet. Therefore, a ML-assisted heat transfer modelling is established for the temperature evolution in the DGR.

1.3. Full-scale emplacement experiment at Mont Terri

Currently, the DGR is the preferred solution for the disposal of the HLW in many countries [6,7,16], such as Switzerland [26]. The proposed concept for a Swiss DGR is shown in Fig. 1 [27] and represents a design concept for a combined repository for low-level and long-lived intermediate-level waste (L/ILW) and for HLW. According to this concept, heat generating HLW canisters emplacement will be along long disposal tunnels. Within the framework of the radioactive waste disposal program in Switzerland, the FE experiment in the Mont Terri URL has been implemented on a 1:1 scale with respect to the tunnel and HLW canister geometries. The FE experimental setup represents different phases of the construction, waste emplacement, backfilling and early evolution of a SF/HLW disposal tunnel of the DGR as realistically as possible [28].

For this purpose, a 50 m long experimental tunnel was constructed as shown in Fig. 2. The tunnel contains a 12 m long interjacent sealing section (ISS) at its deep end. On top of bentonite block pedestals, three identical heaters with dimensions similar to those of HLW canisters (4.6 m long), were emplaced in the FE tunnel. Upon completion of the instrumentation and installation of the monitoring equipment, the remaining space was backfilled with highly compacted granulated bentonite material (GBM). The block pedestals, the GBM and the ISS jointly comprise the bentonite buffer material, which is part of the engineered barrier system (EBS), and thus also part of the multi-barrier concept contributing to the isolation and containment of the radioactive waste [8]. The experiment collects monitoring data, e.g., for monitoring the temperature evolution in the near-field. These data could be used for the model development and validation, initially for the FE experiment and later on applied to a real DGR setup, where the decay heat released by the SF or HLW causes a temperature increase in the bentonite buffer.

The temperature evolution of the buffer material (bentonite block pedestals, GBM, ISS, etc.) depend on its design thermal parameters like the thermal conductivity, density and saturation degree [29]. The inflow of the groundwater from the host rock influences the saturation degree [10] and the thermal conductivity of the GBM. This defines, amongst other parameters, the peak temperature of the buffer material, which is a critical design criterion of the DGR [11]. For the DGR in Switzerland the design criterion is that the maximum temperature of the buffer material is below 140 °C [30]. Higher temperatures can lead to unfavourable material properties of the main component bentonite, and thus influence the overall safety of a DGR [6]. Hence, an accurate estimation of

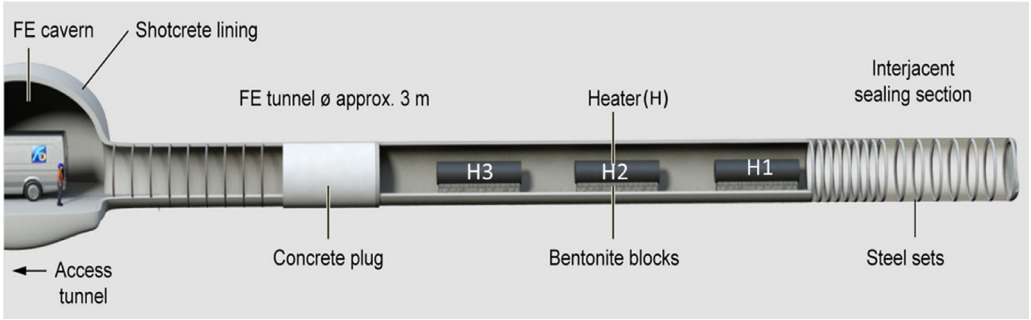

Fig. 2. Illustration of FE tunnel with a scale ratio of 1:1 (without backfill) [8]. (For interpretation of the references to color in this figure legend, the reader is referred to the web version of this article.)

the temperature evolution of the buffer material of the DGR is essential to maintain the performance as well as the safety, economy, reliability of the DGR.

For the FE experiment at Mont Terri URL in Switzerland, there are a lot of temperature sensor data available, however, much less saturation and other hydraulic sensor data, which makes a pure physically based TH modelling difficult to be verified by the available sensor data. Yet, predictive models for the TH evolution of the near-field is essential for the safety analysis of HLW repositories, also to demonstrate system understanding. Furthermore, such models are the basis for the repository construction and monitoring design, their optimization and for the decision support for repository closure. Multiscale modelling is required to cover necessary space and time scales, which is quite challenging because effects of thermal gradients between barrier materials and host rocks, geo-chemical interaction at their interfaces and related changes of their material properties, have to be considered. Here, within the foreseen TH framework, the less dense experimental data for saturation degree are adopted for the NN and physically based surrogate model, whereas heat transport is treated by a pure physical heat transport model. The main driving force of this approach is to speed up these calculations using a fast NN and physically based surrogate model, which replaces the H in the purely physically based TH calculations for the FE experiment [31].

Hence, the experimental data such as the saturation degree are adopted for the ML-based surrogate model, which has been chosen from a variety of NN methods with the best performance. In case of the FE experiment at Mont Terri URL, there are hundreds of sensors which generate tens of thousands values per day. For the facility like the FE experiment, large numbers of sensors as well as even larger amount of the dataset need to be handled, monitored and evaluated. Therefore, the following emerging issues need to be addressed for the ML-assisted heat transport modelling within the DGR: (1) fast and reliable calculation of temperature; (2) performances of different NN methods; (3) validation of results within the ML-assisted modelling framework; (4) comprehensive analysis including the parameters uncertainties and sensor data assessment.

1.4. Scope of this paper

A machine learning (ML)-assisted heat transport modelling framework in the vicinity of a HLW like tunnel is developed and verified with the sensor data from the Full-scale Emplacement (FE) experiment. In Section 2, the physical heat transport model, physically and NN based surrogate model of the thermal conductivity of the granulated bentonite material (GBM), material properties of FE experiment, experiment sensor setup in FE experiment and calculation cases setup are presented within the ML-assisted modelling framework. In Section 3, the ML performance, domain/mesh size determination, model validation, and applications with the ML-assisted modelling framework. Section 4 comes to conclusions and future comments.

2. Machine learning-assisted modelling framework

The developed ML-assisted heat transport modelling framework is illustrated in Fig. 3. The physical model concerns heat transport taking into account the geometrical setup of the tunnel, heater, backfill, and host rock geometry, including materials properties and boundary conditions for heat transport. Hydraulic parameter influencing the heat transport are represented by a surrogate model, which delivers the time and space dependant saturation degree for the thermal conductivity of the GBM. The thermal conductivity of the GBM is the most varying parameter (see Section 3.4.1) due to the resaturation process and the GBM includes most sensors (see Section 2.4). This distribution is obtained from time and space dependant experimental sensor data, which are used to feed a physical supported NN model and replaces a physical hydraulic model for resaturation and related time dependant thermal conductivity of the GBM. The time and space dependant surrogate model for resaturation assists the physical heat transport model yielding saturation degree and related thermal conductivity of the GBM as a function of time and space as learned from time and space dependant saturation (sensor) data. In addition, the material properties of the FE experiment components (Section 2.3), the experimental sensor setup (Section 2.4) and the procedure to determine dominant heat transport parameters for the FE experiment (Section 2.5), are presented in this chapter.

2.1. Heat transport model and setup

The physical heat transport model describes the temperature evolution of the TH processes of the DGR system [15]. As the heat transport in a porous medium basically is dominated by the heat conduction [11,32], the following heat transport equation is solved for the physical modelling.

$$-\lambda_i\left(\frac{\partial^2 T}{\partial x^2}+\frac{\partial^2 T}{\partial y^2}+\frac{\partial^2 T}{\partial z^2}\right)+\rho_i C_{P,\,i}\frac{\partial T}{\partial t}+Q=0, \tag{1}$$

where λ_i is the thermal conductivity of the medium *i; T* is the temperature; *x, y, z* are the coordinates correspondingly; ρ_i is the dry density of the medium *i*; $C_{P,\,i}$ is the specific heat of the medium *i;* Q is the specific heat source.

2.1.1. Initial conditions

From Eq. (1), the dry density ρ_i and thermal conductivity λ_i are two important physical parameters, which are time and space dependant for FE experimental conditions. The initial density profile of the GBM has been measured during the experiment setup

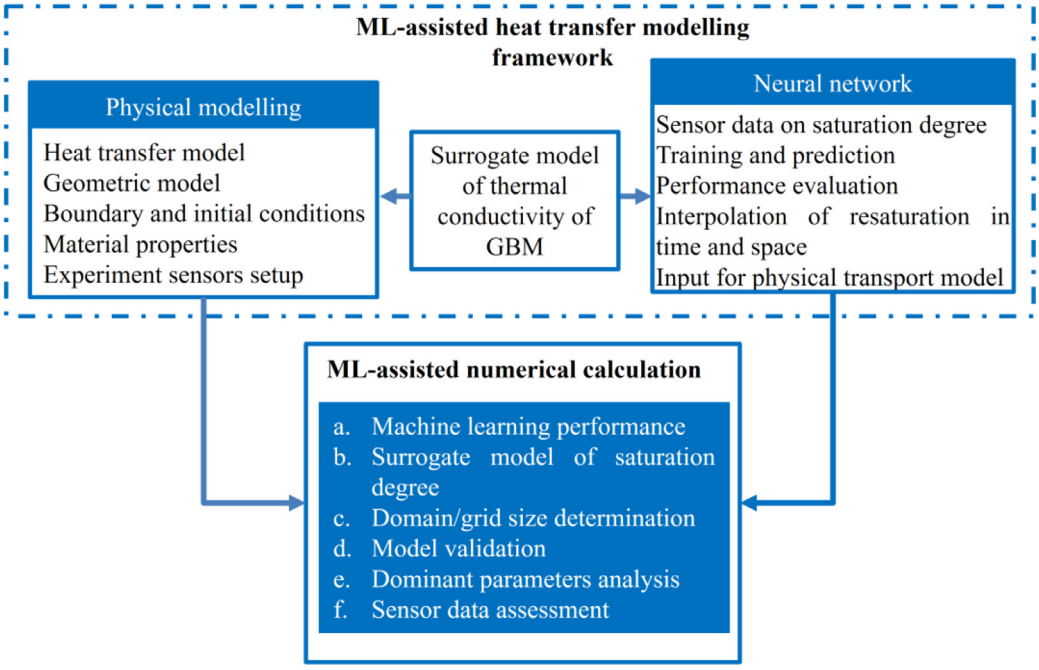

Fig. 3. Illustration of the ML-assisted heat transfer modelling framework. (For interpretation of the references to color in this figure legend, the reader is referred to the web version of this article.)

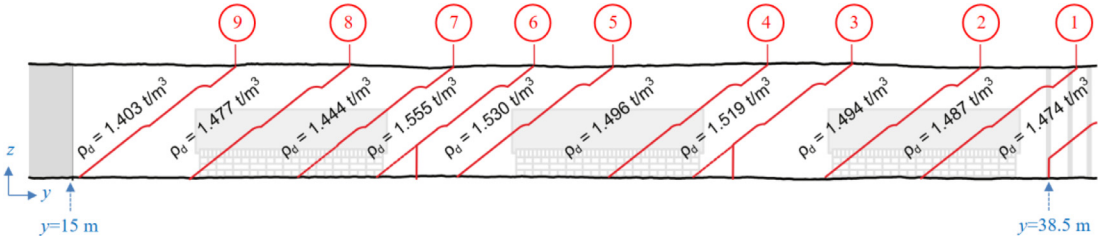

Fig. 4. 3D slope scans and bulk dry densities of the GBM along the backfilled FE tunnel [31]. (For interpretation of the references to color in this figure legend, the reader is referred to the web version of this article.)

[31] and is shown in Fig. 4. The tunnel volume around the heaters and in the gaps between heaters was filled with GBM by a specially designed back-filling augur machine. The dry density $\rho_{GBM,i}$ (ρ_d) of different sections of the GBM varies initially in space and later on with time according to occurring resaturation. In total, 9 slope cans and thus dry density of 10 sections of the GBM are described in Fig. 4. Therefore, the modelling will take this information of the density profile of the GBM into consideration.

A temperature of 19 °C was assumed for the heater, EDZ, concrete plug, bentonite block pedestals, shotcrete and concrete base as well as the GBM as initial temperature for material within the tunnel, whereas a temperature gradient in the clay host rock of 0.06 °C/m [8] yield an initial temperature at the top and bottom surface of the clay host rock of 14 °C and 20 °C, respectively.

2.1.2. Boundary conditions

The specific heat source Q for each heater is also adopted for the analysis for the physical modelling as shown in Eq. (2).

$$Q = P/V, \tag{2}$$

where P is the heater power; V is the heater volume.

These temperature boundary conditions at the top and bottom surface of the model domain were fixed at 14 °C and 20 °C, respectively as boundary conditions, assuming that during the FE experiment temperatures at the top and the bottom of the clay host rock will not be changed. In addition, for four lateral sides of the model domain adiabatic boundary conditions have been assumed, indicating that the model domain has been chosen for a conservative analysis [33]. Finally, the heat power of the three heaters was defined as a boundary condition as shown in Fig. 5. In Fig. 5, the heater 1 shows a ramp switch on, heater 2 shows one step switch on and heater 3 has initially several power interruptions. In total, the experimental time covers the first 548 days of the FE experiment from 15 December 2014 to 15 June 2016 [15].

2.1.3. Geometry model setup

A 3D geometric model of the FE experiment has been generated with the COMSOL Multiphysics software as shown in Fig. 6. It consists of a mesh of more than 1 million nodes and includes the FE cavern, the buffer materials, concrete plug, sections of the GBM, ISS, BBW, the porous concrete, and the far field clay and near filed clay host rock, as well as three heaters, the bentonite block pedestals, the Excavation Damage Zone (EDZ), shotcrete and concrete base (below the bentonite block pedestals) [9]. The density profile of the GBM as shown in Fig. 4 was implemented in the numerical model (Fig. 6(b)). Variable thicknesses of the shotcrete and EDZ and related varying tunnel cross section are ignored for simplicity.

2.2. Surrogate model of thermal conductivity of GBM

In contrast to the common description of TH processes using the Richards equation [10], here the hydraulic processes occurring (mainly) in the buffer material, i.e. resaturation of the bentonite material by water inflow from the host rock, are described

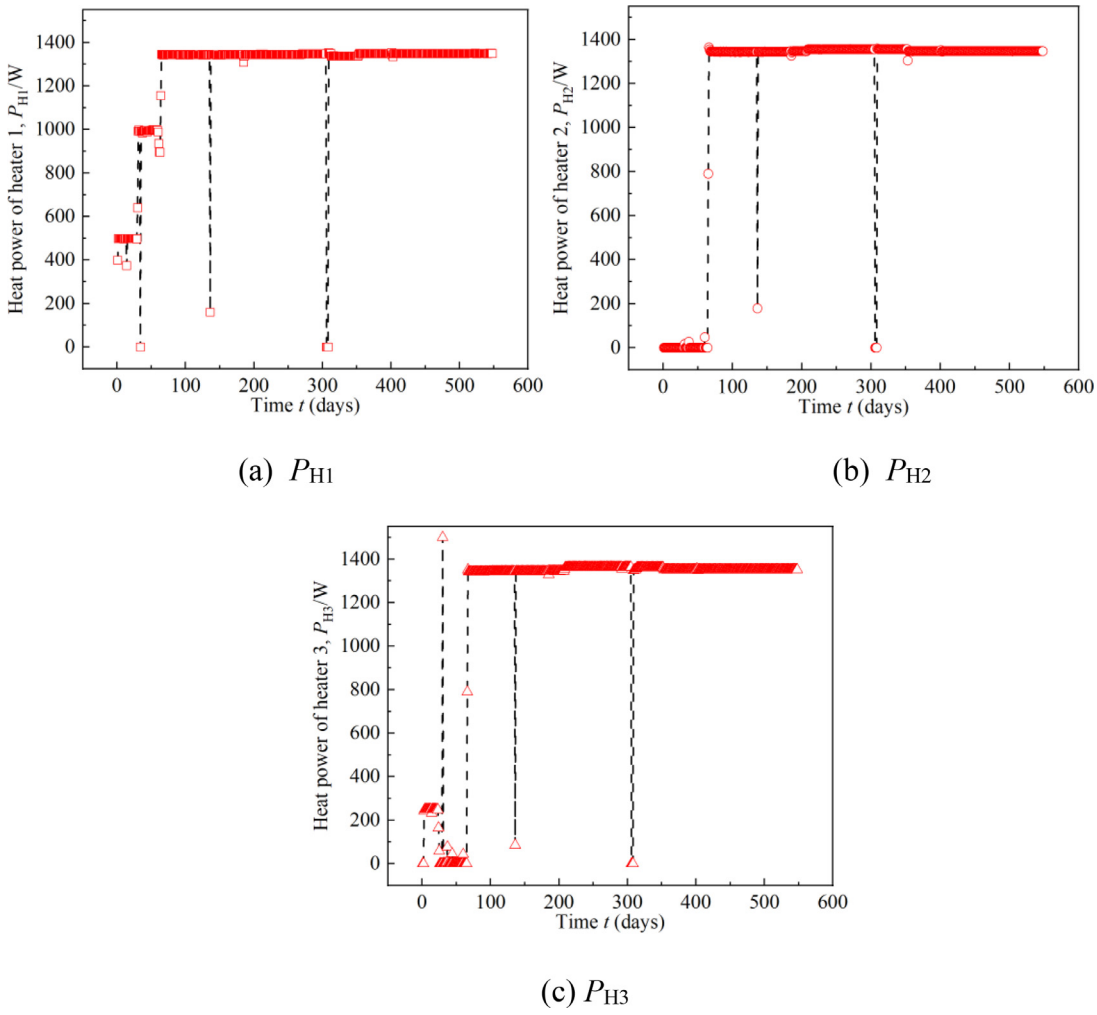

Fig. 5. Boundary conditions with heat power of three heaters (P_{H1}, P_{H2}, P_{H3}) from 15 December 2014 to 15 June 2016 (548 days). (For interpretation of the references to color in this figure legend, the reader is referred to the web version of this article.)

by a surrogate model based on measured saturation data. Using a commonly coupled TH model would be very time-consuming and relatively challenging [16,34], because, if using the coarsely measured water saturation data in a quite heterogeneous buffer material environment and related the strongly non-linear relationship between water saturation and hydraulic conductivity [35], a stiff and slow convergent TH model would be the result.

With lessons learned from Birkholzer et al. (2019) [22], the NN and surrogate models can facilitate complementary modelling and data analysis approaches. Different from the NN applications related to DGRs [21,23–25], we use a physically and NN based surrogate model for the H part and physical heat transport model for the T part. By coupling the physical constraints with NN methods for the surrogate model, the calculation performance of the modelling framework can be enhanced [19,21].

2.2.1. Data preparation with raw dataset

In order to enhance the performance of the ML, a suitable datasets from various sensors should be prepared to train the NN [36]. In practice, some data are missing or abnormal due to sensors failure. Hence, some data preparations such as normalization [37], possible extension [38] and robust NN methods [39] for the experimental dataset have to be taken to treat the raw datasets.

Data were normalized by subtracting the mean value μ of each dataset and divided by the standard deviation σ ($\sigma = 1$ in this section). The normalization of the input raw datasets with zero-mean and constant standard deviation has been proven to be beneficial for NN training [37]. The datasets treated this way include the coordinates, time and temperature, which give the desirable performance of the NN and deal with abnormal values [38]. Three robust NN methods are tested to effectively handle the prepared data [39]: such as the back propagation (BP), cascade back propagation (CBP), Elman NN. The NN methods are tested intensively with our dataset to select the most robust and best performing method.

Applying the above three measures for the data preparation [37–39], a dataset with 20 pairs of temperature and saturation sensors, are used for the NN training. These data were taken at 548 days (from 15 December 2014 to 15 June 2016) for 20 sensors (sensor #1∼#20) with one data point per day, resulting in 10,960 sets of data points in total. Each dataset includes 6 dimensions, the coordinates x, y, z, time t, temperature T and saturation degree S. The former 5 parameters (x, y, z, t, T) are the input parameters, while the latter parameter (S) is the output parameter. Hence, a dataset with the dimension of 10,960 $\times$ 6 is set as the dataset for the ML. 70% of the data are used for training, and the remaining 30% are used for testing [40].

2.2.2. Neural network methods for saturation degree

The NN based ML surrogate model is developed explicitly for the FE experimental setup and is related to the measured sensor

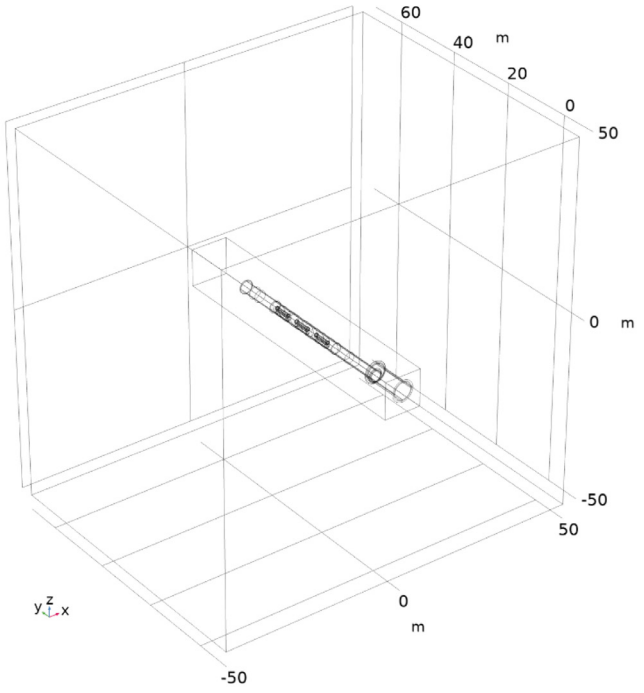

(a) 3D perspective view

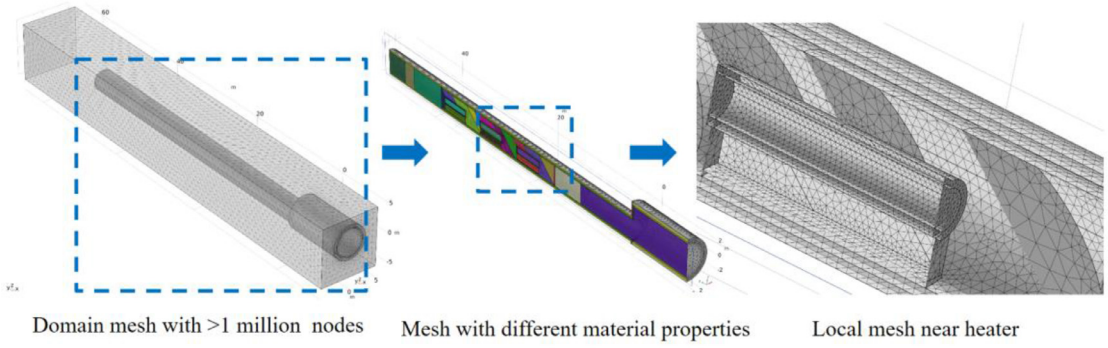

(b) Enlarged view with discretization according to material properties (layers of density profile are shown in local mesh near heater according to Fig. 4)

Fig. 6. Perspective view and enlarged view of 3D geometric model of the FE experiment. (a) 3D perspective view. (b) Enlarged view with discretization according to material properties (layers of density profile are shown in local mesh near heater according to Fig. 4). (For interpretation of the references to color in this figure legend, the reader is referred to the web version of this article.)

data on humidity/saturation (see Fig. 7) depending on sensor location (coordinates and material) and time. The NN methods (BP [41] (Fig. 7(a)), CBP [42] (Fig. 7(b)) and Elman NN [43] (Fig. 7(c)) tested with our dataset are explained in Fig. 7, where w and b represent the weights and biases, respectively. In the BP and CBP, the green arrows represent the connections between the neurons. Each arrow represents a weight w, which is a numerical value that determines the strength of the connection between two neurons. The weights are adjusted during the training process using the backpropagation algorithm or the cascade correlation algorithm, respectively, to minimize the error between the predicted output and the actual output. In an Elman NN, 0 represents the input layer where the external inputs to the network are provided. In addition, 1 represents the hidden layer where the neurons in this layer are connected to the input layer and to themselves from the previous time step. The green arrows in Fig. 7(c) represent the connections between neurons in the current time step and the previous time step.

2.2.3. Neural network performance assessment

To test the performance of the three NN methods described above, three performance evaluation indicators such as the Pearson's r coefficient (R), mean squared error (MSE) and mean absolute error (MAE) are calculated to assess the NN performance [44]. These performance indicators are defined as follows.

$$R = \frac{\sum_{i=1}^{N}(y_{\mathrm{exp,i}} - \overline{y_{\mathrm{exp}}})(y_{\mathrm{pred,i}} - \overline{y_{\mathrm{pred}}})}{\sqrt{\sum_{i=1}^{N}(y_{\mathrm{exp,i}} - \overline{y_{\mathrm{exp}}})^2 \sum_{i=1}^{N}(y_{\mathrm{pred,i}} - \overline{y_{\mathrm{pred}}})^2}}, \tag{3}$$

$$\mathrm{MSE} = \frac{1}{N}\sum_{i=1}^{N}(y_{\mathrm{exp,i}} - \overline{y_{\mathrm{pred,i}}})^2, \tag{4}$$

$$\mathrm{MAE} = \frac{1}{N}\sum_{i=1}^{N}(y_{\mathrm{exp,i}} - \overline{y_{\mathrm{pred,i}}}), \tag{5}$$

where N is the amount of the test dataset; y_{exp} is the experimental dataset; y_{pred} is the prediction dataset.

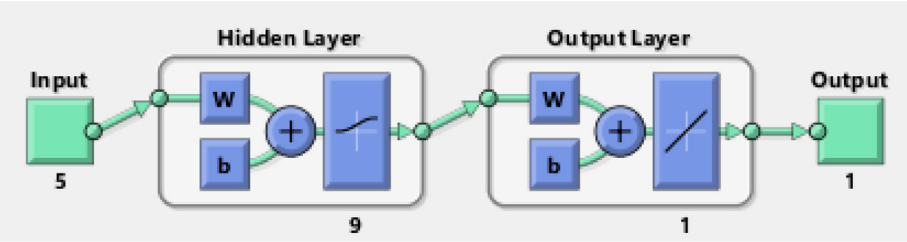

(a) Back propagation

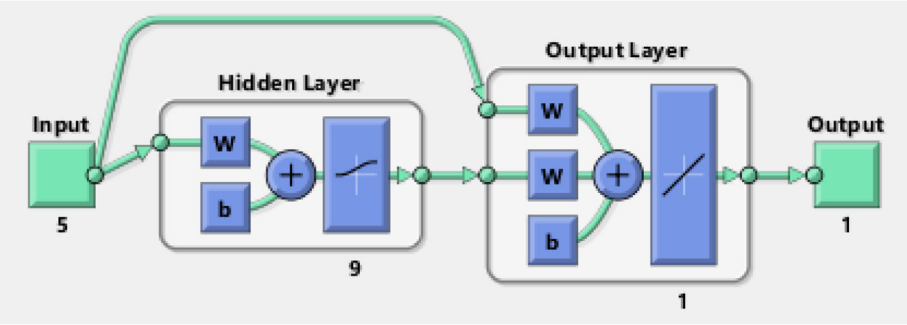

(b) Cascade back propagation

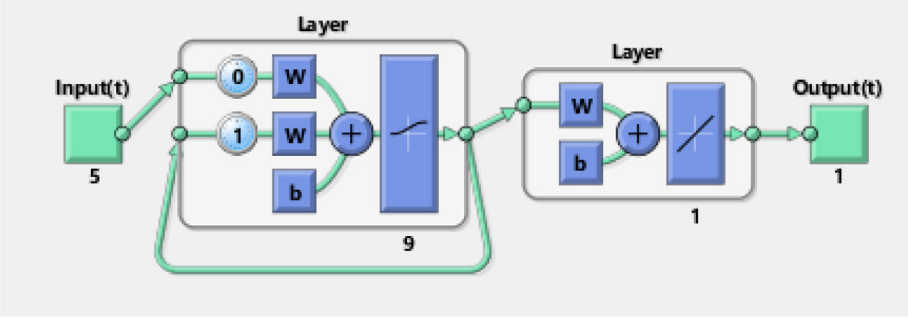

(c) Elman

Fig. 7. Different structures of three neural network methods for saturation degree using Matlab, *w* and *b* represent the weights and biases, 5 input parameters (*x, y, z, t, T*), 9 hidden layers, 1 output layer, 1 output parameter (*S*). (For interpretation of the references to color in this figure legend, the reader is referred to the web version of this article.)

In the above equations, the Pearson's r coefficient R is used to calculate the linear correlation of the prediction dataset and the experimental dataset within the test dataset. It varies from −1 to 1 which represents the degree of the linear correlation. As defined, the MSE reflects the degree of the approximation. The MAE calculates the average errors between two dataset and characterizes the accuracy of the prediction dataset.

2.2.4. Physically and NN based surrogate model

With the above dataset produced by both the sensor data and NN method, a 3D distribution of the saturation degree is determined. Five parameters (*x, y, z, t, T*) are considered for the saturation degree. Other methods such as the Kriging method can hardly can handle data fitting functions for more than three parameters [45].

The resaturation of the GBM, i.e., its saturation degree, is influenced by the inflow of the groundwater from the host rock [10]. Water enters the cylindrical tunnel from the host rock, therefore, the saturation degree should be symmetric in the *x, z* direction in Fig. 6(a) (ignoring advection because of low permeability). Considering the three heaters distributed in the *y*-axis direction, the saturation degree decreases with the distance from heaters. Hence, a sinusoidal function with respect to the position along the tunnel axis is proposed (Eq. (6)). Because of the effect of the gravity, the saturation degree increases with the decrease of the z direction. The saturation monotonously varies with the time t and temperature T. Considering the density profile (see Fig. 4), the experimental data (see Table 4), the NN based saturation degree (see Section 2.2.2), heater locations, time evolution, water resaturation and gravity, the fitting parameters of $a_1 \sim a_5$, $b_1 \sim b_5$ are determined with Eq. (6).

$$S = \left(a_1\sqrt{x^2+z^2}+b_1\right)\cdot\{a_2\sin[2\pi/L(y-\varphi)]+b_2\}\cdot(a_3z+b_3) \cdot(a_4t+b_4)\cdot(a_5T+b_5), \quad (6)$$

where a_1, b_1, a_2, b_2, a_3, b_3, a_4, b_4, a_5, b_5 are parameters which are obtained by the fitting dataset; L is the distance of heaters centerlines, L = 7.6 m for FE tunnel; φ is the centerline location of the heater 1 in the y-axis direction, φ = 35.5 m for FE tunnel.

According to Bai et al. [10], bentonite thermal conductivity $\lambda_{GBM,i}$ can be described as a function of bentonite density and saturation degree S (Eq. (7), where $\rho_{GBM,i}$ represents the bentonite density in the different GBM sections i along the tunnel and $\lambda_{GBM,i}$ is the related thermal conductivity in section i (see Fig. 4). Thus, the influence of the hydraulic parameter saturation degree S on the thermal parameter $\lambda_{GBM,i}$ is directly taken into account, cou-

Table 1
Physical parameters of typical material of EBS in FE.

Physical parameters	Value	Ref.
Thermal conductivity of EDZ λ_{EDZ} ($W{\cdot}m^{-1}{\cdot}K^{-1}$)	2.4 (H)/1.3 (V)	[8]
Thermal conductivity of bentonite block λ_{block} ($W{\cdot}m^{-1}{\cdot}K^{-1}$)	0.7 (0.26∼0.96)	[47]
Thermal conductivity of clay λ_{clay} ($W{\cdot}m^{-1}{\cdot}K^{-1}$)	2.4 (H)/1.3 (V)	[8]
Thermal conductivity of concrete $\lambda_{concrete}$ ($W{\cdot}m^{-1}{\cdot}K^{-1}$)	0.2 (0.1∼0.3)	[8]
Thermal conductivity of heater canister $\lambda_{canister}$ ($W{\cdot}m^{-1}{\cdot}K^{-1}$)	50	*
Density of EDZ ρ_{EDZ} ($kg{\cdot}m^{-3}$)	2340	[8]
Density of bentonite block ρ_{block} ($kg{\cdot}m^{-3}$)	1780	[48]
Density of clay ρ_{clay} ($kg{\cdot}m^{-3}$)	2340	[8]
Density of concrete $\rho_{concrete}$ ($kg{\cdot}m^{-3}$)	2300	[8]
Specific heat of EDZ $C_{P,EDZ}$ ($J{\cdot}kg^{-1}{\cdot}K^{-1}$)	1086	[8]
Specific heat of bentonite block $C_{P,block}$ ($J{\cdot}kg^{-1}{\cdot}K^{-1}$)	800	[48]
Specific heat of clay $C_{P,clay}$ ($J{\cdot}kg^{-1}{\cdot}K^{-1}$)	995	[8]
Specific heat of concrete $C_{P,concrete}$ ($J{\cdot}kg^{-1}{\cdot}K^{-1}$)	750	[8]
Specific heat of GBM $C_{P,\,GBM}$ ($J{\cdot}kg^{-1}{\cdot}K^{-1}$)	800	[8]

where H and V represent values in the horizontal and vertical directions respectively; Ref. represents "Reference"; * means an assumption value.

pling the TH processes according to

$$\lambda_{GBM,i} = a \cdot \rho_{GBM,i} + b \cdot S + c, \tag{7}$$

where *a, b* are the fitting parameters related to the bentonite density $\rho_{GBM,i}$ and the saturation degree *S*, respectively; and *c* is the fitting constant according to [46] ($a = 0.641$, $b = 0.624$, $c = -0.510$).

2.3. Material properties of FE experiment components

The physical parameters of the materials in the EBS of the FE experiment like the EDZ, bentonite block pedestals, etc. are summarized in Table 1. Particularly, the horizontal (H) and vertical (V) directions of the anisotropic thermal conductivities of the EDZ λ_{EDZ} and of the clay λ_{clay} are considered and the inclination of the bedding plane is considered. The concrete material properties in Table 1 represent the shotcrete and concrete base. Similarly in Table 1, the bentonite block properties represent the bentonite block pedestals and the bentonite block wall (BBW) properties.

For all materials in Table 1, constant specific heat capacities, densities and thermal conductivities of the EDZ, concrete and bentonite block are assumed to decouple the calculation from the heat transport model. This is also consistent with details given in [31]. Although the thermal properties of the EDZ, concrete and bentonite block may slightly change with temperature, their values are kept for modelling. Only minor effects on the temperature evolution of the buffer material in the FE experiment are observed and shown in Section 3.1 within the model validation procedure. As mentioned above, the thermal conductivity of each section of the GBM changes with the time and space while the specific heat of the GBM is kept constant. It should be mentioned that the constant values of the physical parameters in Table 1 are used for the validation of the physical model, while variation ranges of these parameter values have been used to identify dominating parameters.

2.4. Experimental sensor setup

The sensors installed for FE experiment should yield a dataset representative of the early stage evolution of a HLW repository tunnel enabling comparison with modelling approaches and calculation analysis of the FE experiment. During the initial phase of the FE experiment, some of the installed sensors showed already failures [9]. Therefore, representative sensors (20 + 20 + 10 = 50 sensors) at various cross-section (which are mainly focused on in the report [15]) are selected for the calculation analysis shown in Fig. 8.

Table 2
Corresponding sensors ID and 20 pair-sensors of temperature and saturation degree.

No	ID of temperature sensor	ID of saturation degree sensor	*x*/m	*y*/m	*z*/m
#1	T-BH2–230_1	RH–H2–230_1	0.293	27.9	0.514
#2	T-H3–230-O_4	RH–H2–230_2	0.608	27.9	−0.022
#3	FE_TEM_108	FE_HUM_020	1.036	27.9	0.889
#4	FE_TEM_109	FE_HUM_021	−0.707	27.9	1.283
#5	FE_TEM_110	FE_HUM_022	0.911	27.9	0.772
#6	FE_TEM_111	FE_HUM_023	−0.625	27.9	1.139
#7	FE_TEM_106	FE_HUM_018	0.939	28.9	0.814
#8	FE_TEM_107	FE_HUM_019	−0.623	28.9	1.131
#9	FE_TEM_098	FE_HUM_012	1.003	31.25	0.851
#10	FE_TEM_100	FE_HUM_014	−0.698	31.25	1.238
#11	FE_TEM_101	FE_HUM_015	0.882	31.25	0.723
#12	FE_TEM_103	FE_HUM_017	−0.62	31.25	1.083
#13	FE_TEM_094	FE_HUM_008	1.056	35.22	0.886
#14	FE_TEM_095	FE_HUM_009	−0.704	35.22	1.224
#15	FE_TEM_096	FE_HUM_010	0.93	35.22	0.756
#16	FE_TEM_025	FE_HUM_025	−0.027	23.9	−1.257
#17	FE_TEM_105	FE_HUM_027	0	23.9	−1.113
#18	FE_TEM_013	FE_HUM_013	−0.011	31.25	−1.281
#19	FE_TEM_016	FE_HUM_016	−0.004	31.25	−1.131
#20	T-BH1–230_1	RH-H1–230_1	0.318	35.22	0.512

Corresponding sensors identify-number (ID) and typical 20 pairs of temperature/saturation degree sensors (20 + 20 = 40 sensors) are included in Table 2. These pairs of temperature/saturation degree sensors record the experimental datasets of temperature and saturation degree at the same positions. Sensor pairs are mainly distributed in the upper half of the GBM (sensor #1∼#16, red dot series) [15] as shown in Fig. 8. In the lower half of the GBM, there are just 4 pairs of sensors (sensor #17∼#20, black dot series) related with the temperature/saturation degree. There are not enough sensors in the lower part of the experiment to adequately describe the saturation. Therefore, we are using a NN based surrogate model to predict the saturation degree and use it as input for the heat transport modelling.

For model validation, corresponding sensors ID and 10 temperature sensors of the green dot series in Fig. 8 are chosen as representative temperature sensors at different distances from the heater within the GBM in Table 3. Six temperature sensors, e.g., H1–1, H1–2 are near the GBM-heater surface experience strong initial temperature gradient. Three temperature sensors, including the G1, G2 and G3 within the GBM, are relatively far from three heaters, experiencing moderate temperature gradient, and the temperature sensor C1 is in the clay host rock (out of scale in Fig. 8, and experiences a small temperature gradient.

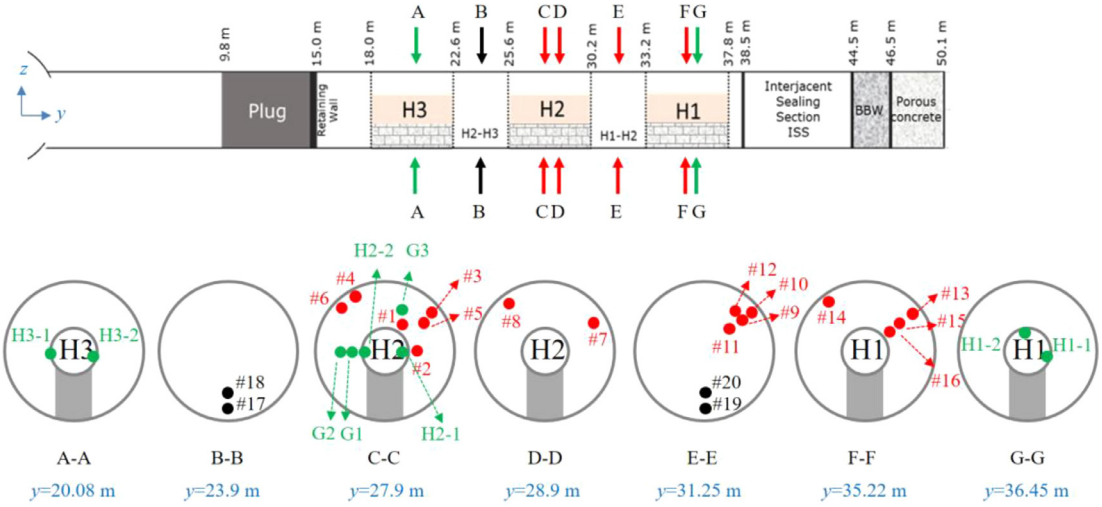

Fig. 8. Schematic diagram of positions of typical 20 pairs of temperature/saturation degree sensors and 10 temperature sensors in the upper and lower half of the GBM and heaters, red dot series of sensors represent pairs of temperature/saturation sensors #1∼#16 within the upper GBM, black dot series of sensors indicate pairs of temperature/saturation sensors #17∼#20 within the lower GBM, green dot series of sensors represent 10 temperature sensors (1 temperature sensor in the clay is not shown). (For interpretation of the references to color in this figure legend, the reader is referred to the web version of this article.)

Table 3
Corresponding sensors ID and 10 temperature sensors for model validation.

Sensor	ID of temperature sensor	x/m	y/m	z/m
H1–1	T-H1–330-O_3	0.523	36.45	−0.043
H1–2	T-H1–330-O_1	−0.057	36.45	0.479
H2–1	T-H2–230-O_3	0.508	27.9	−0.022
H2–2	T-H2–230-O_5	−0.542	27.9	−0.022
H3–1	T-H3–230-O_3	0.505	20.28	−0.026
H3–2	T-H3–230-O_5	−0.545	20.28	−0.026
G1	T-RH-H2–230_4	−0.637	27.9	−0.022
G2	T-BH2–230_4	−0.642	27.9	−0.022
G3	T-BH2–230_6	0.395	27.9	0.692
C1	BFEB006_TEM_01	2.638	27.9	−3.024

2.5. Calculation case setup for dominant parameters analysis

In order to analyse and identify the dominant parameters influencing the heat transport in the FE experiment, the orthogonal test method is selected for the dominant parameters analysis presented in Section 3.3 [49]. It used to dramatically reduce the number of sampling cases. Heat transport processes in the FE experiment are influenced mainly by seven design parameters including the heat power of the three heaters (P_{H1}, P_{H2}, P_{H3}), thermal conductivities of the GBM, the EDZ λ_{EDZ}, the heater canister $\lambda_{canister}$, and the bentonite block λ_{block}.

Table 4 shows seven parameters and their individual ranges investigated, which are covered by 4 parameter values each. Heater power values (P_{H1}, P_{H2}, P_{H3}) are related to initial experimental heater phases, the steady-state value of 1350 W and a potential larger possible value of 1500 W. Values of parameter [λ_{GBM1}, .., λ_{GBM10}] are chosen equidistantly around the values of the validation model of dataset 1.0 × [λ_{GBM1}, .., λ_{GBM10}], where $\lambda_{GBM1-10}$ is related to the thermal conductivities of 10 sections of the GBM as shown in Fig. 4. Values of parameter λ_{EDZ} and $\lambda_{canister}$ are also chosen around the values of the validation model of 2.4 $W{\cdot}m^{-1}{\cdot}K^{-1}$ and 1.3 $W{\cdot}m^{-1}{\cdot}K^{-1}$ in the horizontal and vertical directions, and 50 $W{\cdot}m^{-1}{\cdot}K^{-1}$, respectively, whereas parameter λ_{block} values are chosen according to values given in [8]. From this set of parameter variations, the orthogonal test methods yields a matrix of 32 combinations of input parameter values given in Table 5.

3. Results and discussion

In this section, the results of testing different ML algorithms and their performance are presented, which yield the most robust surrogate model for providing input, 3D thermal conductivity distribution as a function of time, for the physically based heat transport model. To validate the measured temperature sensor data, influences of the domain size/mesh size have been tested for the heat transport model setup to finally reproduce temperature data for 10 representative temperature sensors. Then, the parameter set for the validation model has been used to identify the dominating parameters applying an orthogonal test method with 32 test cases. Latter allows to determine the parameter uncertainty with respect to reliability of sensor data and a predefined uncertainty bandwidth of important model parameter.

3.1. Data preparation and machine learning performance

Sensor data preparation is important for the performance of the NN based ML algorithms. For simplicity and for automation reasons, raw datasets from the FE experiment are handled directly by the NN based ML methods to introduce as less user activity as possible for the data preparation.

The three NN based ML techniques have been tested with the 50%–50%, 60%–40% and 70%–30% train-test datasets, whereby the 70%–30% train-test setup performs best for all ML methods. In Fig. 9, three indicator parameters (see Section 2.2.3) for the performance like the R, MSE and MAE are shown for the three NN based ML techniques. All three NN based ML algorithms perform well with a 70%–30% train-test datasets. The Elman NN operates better than the BP, CBP methods with R = 0.9911, MSE = 4.62 and MAE = 1.44. It should be mentioned that all performance indicators are obtained based on the raw dataset, not the normalized dataset.

3.2. Domain and grid size determination and model validation

To investigate the domain size effect and grid independence, a dataset of 137 × 2 data points for temperature sensors H2–1 and C1 (in the clay) are selected being the nearest and most distant sensor locations from the heat source, respectively. Three domain

Table 4
Parameters and values for orthogonal test cases.

Values	Parameters						
	A, P_{H1} (W)	B, P_{H2} (W)	C, P_{H3} (W)	D, λ_{GBM} ($W{\cdot}m^{-1}{\cdot}K^{-1}$)	E, λ_{EDZ} ($W{\cdot}m^{-1}{\cdot}K^{-1}$)	F, $\lambda_{canister}$ ($W{\cdot}m^{-1}{\cdot}K^{-1}$)	G, λ_{block} ($W{\cdot}m^{-1}{\cdot}K^{-1}$)
1	1050	1050	1050	0.8 × [λ_{GBM1}, .., λ_{GBM10}]	2.0 (H) 1.1 (V)	20	0.3
2	1200	1200	1200	0.9 × [λ_{GBM1}, .., λ_{GBM10}]	2.2 (H) 1.2 (V)	50	0.5
3	1350	1350	1350	1.0 × [λ_{GBM1}, .., λ_{GBM10}]	2.4 (H) 1.3 (V)	80	0.7
4	1500	1500	1500	1.1 × [λ_{GBM1}, .., λ_{GBM10}]	2.6 (H) 1.4 (V)	110	0.9

where the parameter λ_{GBM} is the combination of the thermal conductivity of 10 sections of the GBM; for the parameter λ_{EDZ}, H and V represent values in the horizontal and vertical directions respectively.

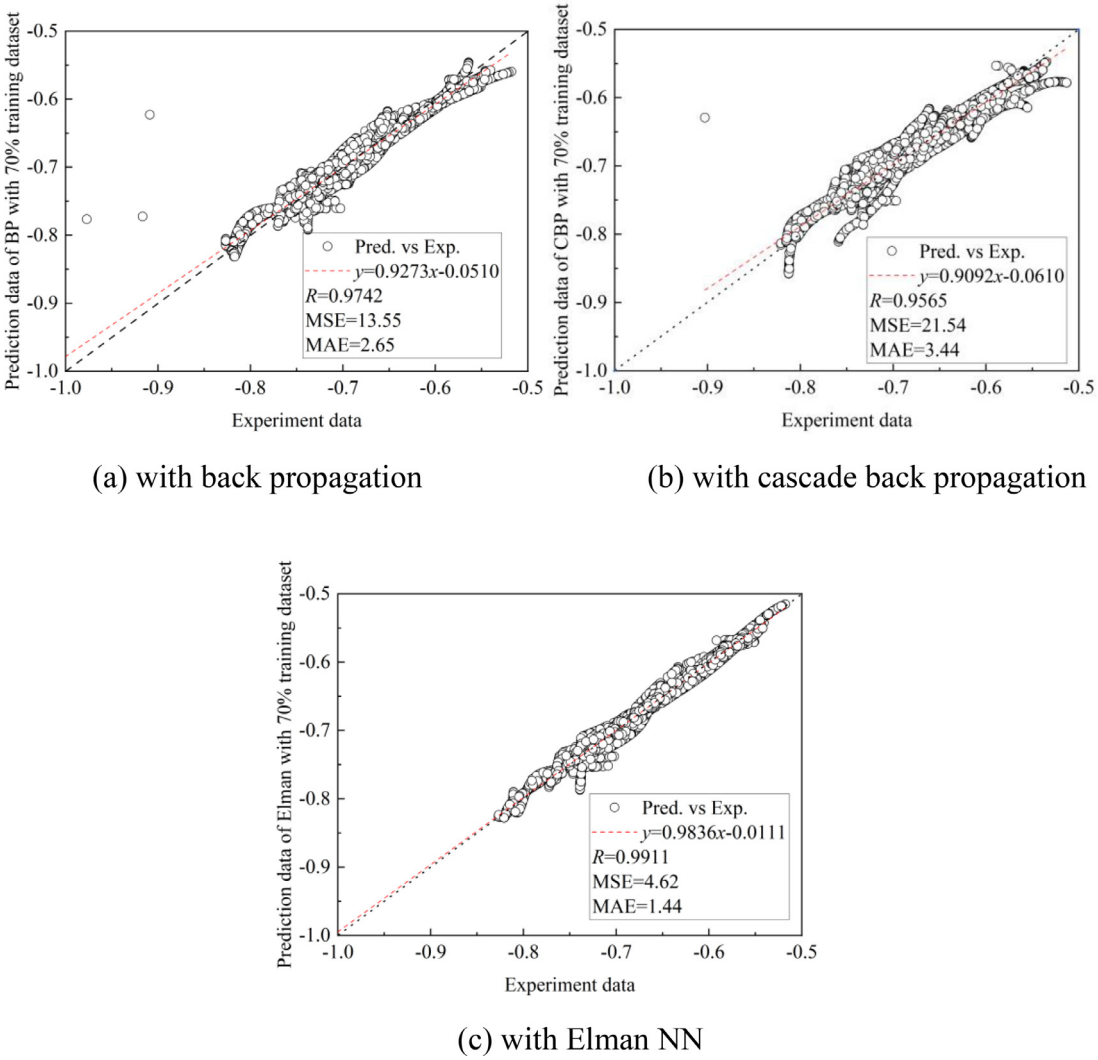

Fig. 9. Comparison of 30% predicted (Pred.) data by BP, CBP and Elman neural network machine learning methods with a 70% input training dataset from the experimental (Exp.) sensor dataset. (For interpretation of the references to color in this figure legend, the reader is referred to the web version of this article.)

sizes and three meshes are calculated at the positions of the sensors H2–1 and C1 during $t = 0{\sim}548$ days correspondingly. The results are shown below for sensor H2–1; those for C1 are shown in Fig. S1 in the Supplementary Material. For validation of the ML-assisted heat transport model, 10 representative temperature sensors data are considered using the determined calculation domain and mesh size.

3.2.1. Domain and grid size determination

For the domain size determination as well as the grid independence analysis, three domain sizes and three meshes are conducted as shown in Table 6. It assures that temperature boundary conditions at the domain boundaries do not influence the model results. For comparison with the modelling results, a dataset with 137 × 2 data points at positions of the temperature sensors

Table 5
Design results of test cases for dominant parameters.

Case	Parameters							Design schemes
	A, P_{H1} (W)	B, P_{H2} (W)	C, P_{H3} (W)	D, λ_{GBM} ($W{\cdot}m^{-1}{\cdot}K^{-1}$)	E, λ_{EDZ} ($W{\cdot}m^{-1}{\cdot}K^{-1}$)	F, $\lambda_{canister}$ ($W{\cdot}m^{-1}{\cdot}K^{-1}$)	G, λ_{block} ($W{\cdot}m^{-1}{\cdot}K^{-1}$)	
1	1050	1050	1050	0.8 × [λ_{GBM1}, .., λ_{GBM10}]	2.0 (H) 1.1 (V)	20	0.3	A1B1C1D1E1F1G1
2	1050	1050	1200	0.9 × [λ_{GBM1}, .., λ_{GBM10}]	2.6 (H) 1.4 (V)	110	0.7	A1B1C2D2E4F4G3
3	1050	1200	1350	1.1 × [λ_{GBM1}, .., λ_{GBM10}]	2.0 (H) 1.1 (V)	50	0.7	A1B2C3D4E1F2G3
4	1050	1200	1500	1.0 × [λ_{GBM1}, .., λ_{GBM10}]	2.6 (H) 1.4 (V)	80	0.3	A1B2C4D3E4F3G1
5	1050	1350	1050	1.0 × [λ_{GBM1}, .., λ_{GBM10}]	2.2 (H) 1.2 (V)	110	0.5	A1B3C1D3E2F4G2
6	1050	1350	1200	1.1 × [λ_{GBM1}, .., λ_{GBM10}]	2.4 (H) 1.3 (V)	20	0.9	A1B3C2D4E3F1G4
7	1050	1500	1350	0.9 × [λ_{GBM1}, .., λ_{GBM10}]	2.2 (H) 1.2 (V)	80	0.9	A1B4C3D2E2F3G4
8	1050	1500	1500	0.8 × [λ_{GBM1}, .., λ_{GBM10}]	2.4 (H) 1.3 (V)	50	0.5	A1B4C4D1E3F2G2
9	1200	1050	1350	1.1 × [λ_{GBM1}, .., λ_{GBM10}]	2.4 (H) 1.3 (V)	110	0.5	A2B1C3D4E3F4G2
10	1200	1050	1500	1.0 × [λ_{GBM1}, .., λ_{GBM10}]	2.2 (H) 1.2 (V)	20	0.9	A2B1C4D3E2F1G4
11	1200	1200	1050	0.8 × [λ_{GBM1}, .., λ_{GBM10}]	2.4 (H) 1.3 (V)	80	0.9	A2B2C1D1E3F3G4
12	1200	1200	1200	0.9 × [λ_{GBM1}, .., λ_{GBM10}]	2.2 (H) 1.2 (V)	50	0.5	A2B2C2D2E2F2G2
13	1200	1350	1350	0.9 × [λ_{GBM1}, .., λ_{GBM10}]	2.6 (H) 1.4 (V)	20	0.3	A2B3C3D2E4F1G1
14	1200	1350	1500	0.8 × [λ_{GBM1}, .., λ_{GBM10}]	2.0 (H) 1.1 (V)	110	0.7	A2B3C4D1E1F4G3
15	1200	1500	1050	1.0 × [λ_{GBM1}, .., λ_{GBM10}]	2.6 (H) 1.4 (V)	50	0.7	A2B4C1D3E4F2G3
16	1200	1500	1200	1.1 × [λ_{GBM1}, .., λ_{GBM10}]	2.0 (H) 1.1 (V)	80	0.3	A2B4C2D4E1F3G1
17	1350	1050	1350	0.8 × [λ_{GBM1}, .., λ_{GBM10}]	2.6 (H) 1.4 (V)	50	0.9	A3B1C3D1E4F2G4
18	1350	1050	1500	0.9 × [λ_{GBM1}, .., λ_{GBM10}]	2.0 (H) 1.1 (V)	80	0.5	A3B1C4D2E1F3G2
19	1350	1200	1050	1.1 × [λ_{GBM1}, .., λ_{GBM10}]	2.6 (H) 1.4 (V)	20	0.5	A3B2C1D4E4F1G2
20	1350	1200	1200	1.0 × [λ_{GBM1}, .., λ_{GBM10}]	2.0 (H) 1.1 (V)	110	0.9	A3B2C2D3E1F4G4
21	1350	1350	1350	1.0 × [λ_{GBM1}, .., λ_{GBM10}]	2.4 (H) 1.3 (V)	80	0.7	A3B3C3D3E3F3G3
22	1350	1350	1500	1.1 × [λ_{GBM1}, .., λ_{GBM10}]	2.2 (H) 1.2 (V)	50	0.3	A3B3C4D4E2F2G1
23	1350	1500	1050	0.9 × [λ_{GBM1}, .., λ_{GBM10}]	2.4 (H) 1.3 (V)	110	0.3	A3B4C1D2E3F4G1
24	1350	1500	1200	0.8 × [λ_{GBM1}, .., λ_{GBM10}]	2.2 (H) 1.2 (V)	20	0.7	A3B4C2D1E2F1G3
25	1500	1050	1050	1.1 × [λ_{GBM1}, .., λ_{GBM10}]	2.2 (H) 1.2 (V)	80	0.7	A4B1C1D4E2F3G3
26	1500	1050	1200	1.0 × [λ_{GBM1}, .., λ_{GBM10}]	2.4 (H) 1.3 (V)	50	0.3	A4B1C2D3E3F2G1
27	1500	1200	1350	0.8 × [λ_{GBM1}, .., λ_{GBM10}]	2.2 (H) 1.2 (V)	110	0.3	A4B2C3D1E2F4G1
28	1500	1200	1500	0.9 × [λ_{GBM1}, .., λ_{GBM10}]	2.4 (H) 1.3 (V)	20	0.7	A4B2C4D2E3F1G3
29	1500	1350	1050	0.9 × [λ_{GBM1}, .., λ_{GBM10}]	2.0 (H) 1.1 (V)	50	0.9	A4B3C1D2E1F2G4
30	1500	1350	1200	0.8 × [λ_{GBM1}, .., λ_{GBM10}]	2.6 (H) 1.4 (V)	80	0.5	A4B3C2D1E4F3G2
31	1500	1500	1350	1.0 × [λ_{GBM1}, .., λ_{GBM10}]	2.0 (H) 1.1 (V)	20	0.5	A4B4C3D3E1F1G2
32	1500	1500	1500	1.1 × [λ_{GBM1}, .., λ_{GBM10}]	2.6 (H) 1.4 (V)	110	0.9	A4B4C4D4E4F4G4

H2–1 and C1 are selected. In Table 6, results for three domain sizes of 50 m × 80 m × 50 m, 100 m × 80 m × 100 m and 150 m × 100 m × 150 m are calculated and shown in Fig. 10(a). In addition, calculations with three different meshes with 1253,142, 1719,617 and 2274,148 nodes are tested. The results are shown in Fig. 10(b).

In Table 6 and Fig. 10(a), the maximum relative errors of calculation results between the domain 1, domain 2 and domain 3 are 1.12%, 0.74%, respectively (compared to domain 3). Similarly in Table 6 and Fig. 10(b), the maximum relative errors of calculation results between the mesh 1, mesh 2 and mesh 3 are 1.79%, 0.99%, respectively (compared to mesh 3). In order to make the trade-

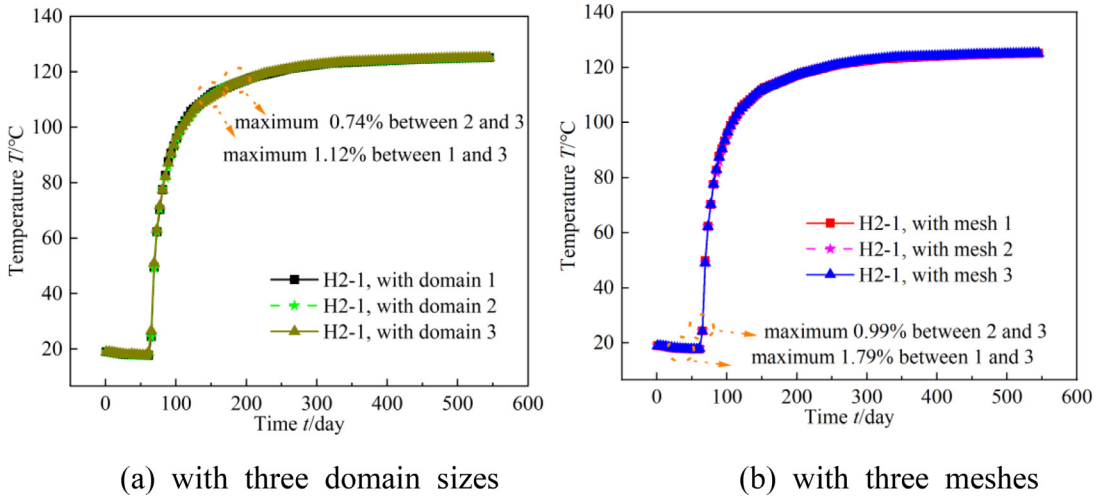

Fig. 10. Comparison of calculation data of at position of sensor H2–1 with (a) three different domain sizes and (b) three different meshes. (For interpretation of the references to color in this figure legend, the reader is referred to the web version of this article.)

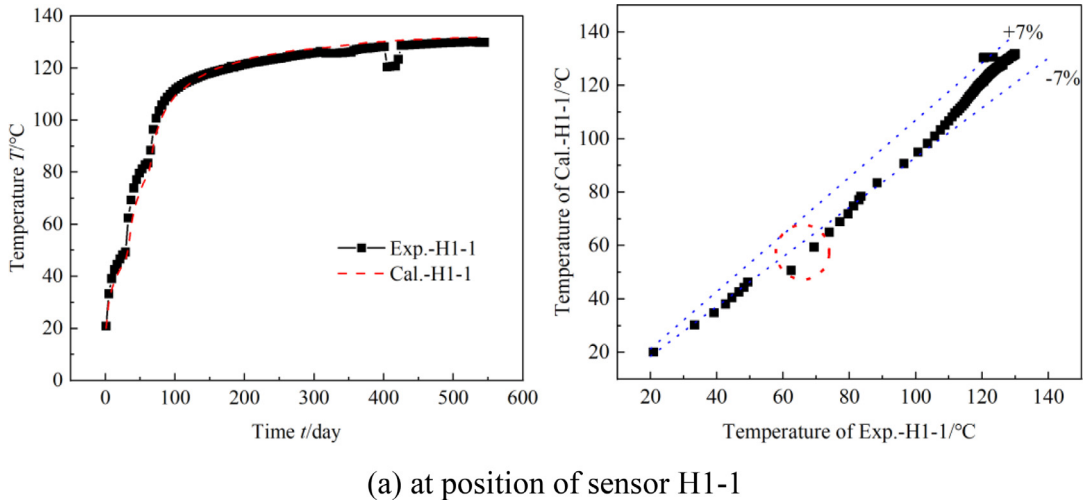

Fig. 11. Comparison of temperature evolution T and relative errors between calculation and experimental data at positions of 10 representative sensors during 1.5 years (t = 0~548 days). (For interpretation of the references to color in this figure legend, the reader is referred to the web version of this article.)

Table 6
Maximum relative errors of sensor H2–1with three domain sizes and three meshes.

Sensor	Size ($x \times y \times z$)	Maximum relative error	Time of maximum error t/day
Domain 1	50 m × 80 m × 50 m	1.12%	153
Domain 2	100 m × 80 m × 100 m	0.74%	165
Domain 3	150 m × 100 m × 150 m	~	~
Mesh 1	1253,142	1.79%	37
Mesh 2	1719,617	0.99%	61
Mesh 3	2274,148	~	~

off between the calculation efforts and accuracy, the domain of 100 m × 80 m × 100 m (domain 2) and mesh size of 1719,617 (mesh 2) are selected for the ML-assisted heat transport modelling for the FE experiment.

3.2.2. Validation of physical model with experimental data

The comprehensive comparison of the temperature evolution T and relative errors between the calculation and experimental data of 10 representative sensors are shown in Fig. 11. The calculation details and the related material properties are given above (see Section 2.2-2.4). For the identification of the "best fit" or validation case parameters, which reproduce the experimental data, also results of Section 3.3 and 3.4 have been used. The chosen experimental data consist of 137 data points for 10 representative temperature sensors each, which are compared with the calculated data time t = 0 to 548 days as shown in Fig. 11. The positions of 10 temperature sensors include sensors near the GBM-heater surfaces, sensors within the GBM and sensor in the host clay. Hence, a large experimental dataset of 137 × 10 data points are taken into account for the model validation. It should be noted that the experiment sensor data are the raw dataset.

Considering that the temperature T near the three GBM-heater surfaces are higher than that in the GBM or clay, the peak temperature near the GBM-heater surfaces are also larger and hence will be more focused. From Fig. 11(a)~(d), except a few data points, the maximum relative errors between the calculation and experimental data at positions of the sensor H1–1, H2–1, H2–1 and H2–2 are within 7.0%. Those few data points with the larger errors occur during the initial transient state which includes stepwise heater power increases and some power interruptions. For sensors H3–1 and H3–2 (Fig. 11(e)~(f)), the maximum relative errors between the calculation and experimental data are within 9.0%. This slightly larger errors might be induced by the abnormal operation of the heater 3, which can be seen in Fig. 7(c) (see Section 2.1.2), where

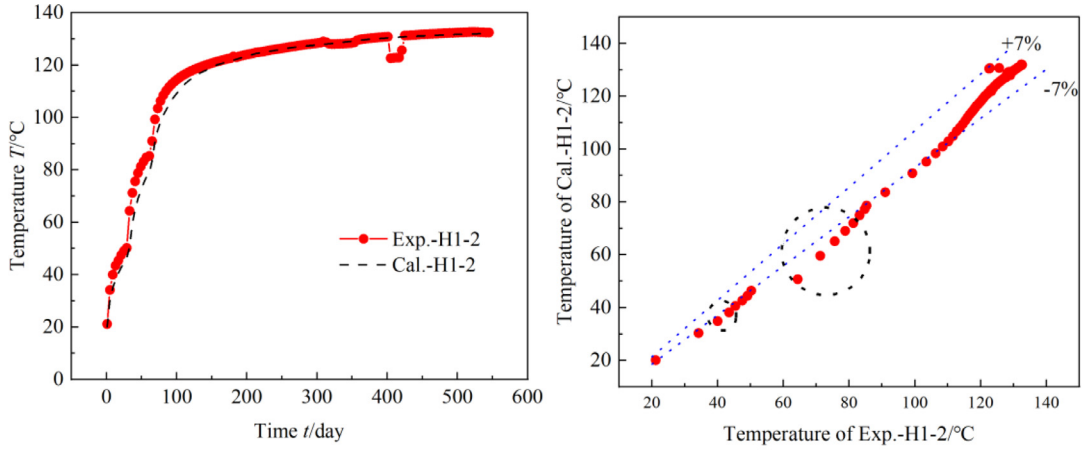

(b) at position of sensor H1-2

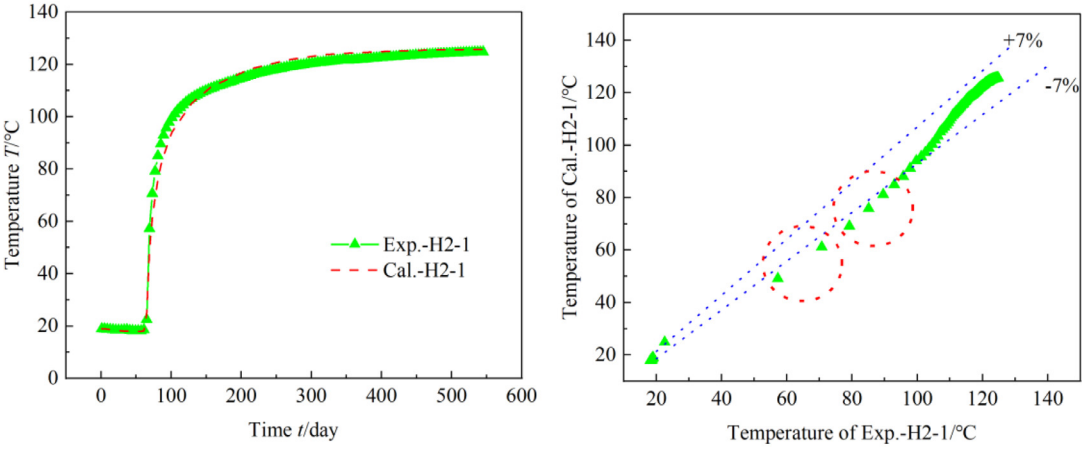

(c) at position of sensor H2-1

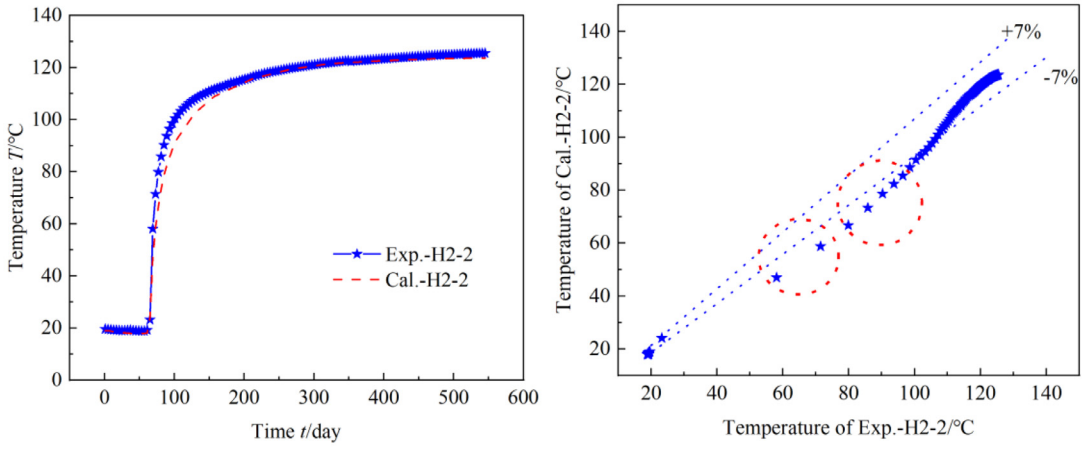

(d) at position of sensor H2-2

Fig. 11. Continued

a peak power of around 1500 W stayed for only 1 day and decrease to nearly zero next day and later on achieving the target value of 1350 W. The maximum relative errors during the transient initial phase reduce to a value lower than 3.5% at later times.

For sensors at larger distance from the heater within the GBM, a similar trend is observed in Fig. 11(g)~(i). The maximum error is within 7% at positions of the sensors G1, G2 and G3 (Fig. 11(g)~(i)). For the most distant sensor C1 in the clay, the relative error between the calculation results and experimental data is within 3% (see Fig. 11(j)). Additionally, the coordinate scale of Fig. 11(j) remains consistent with that in other sensors and presents the magnitude more clearly. For the sensors like the sensor H1–2, H2–2

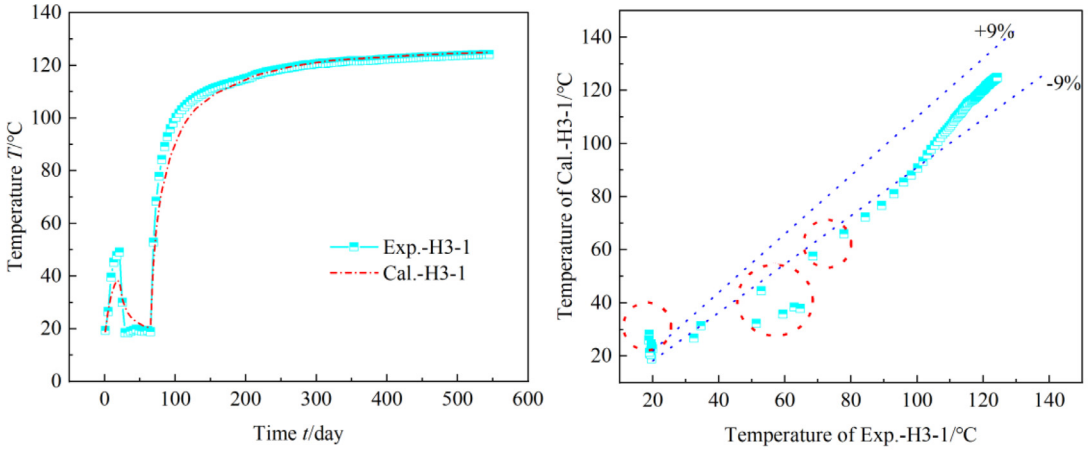

(e) at position of sensor H3-1

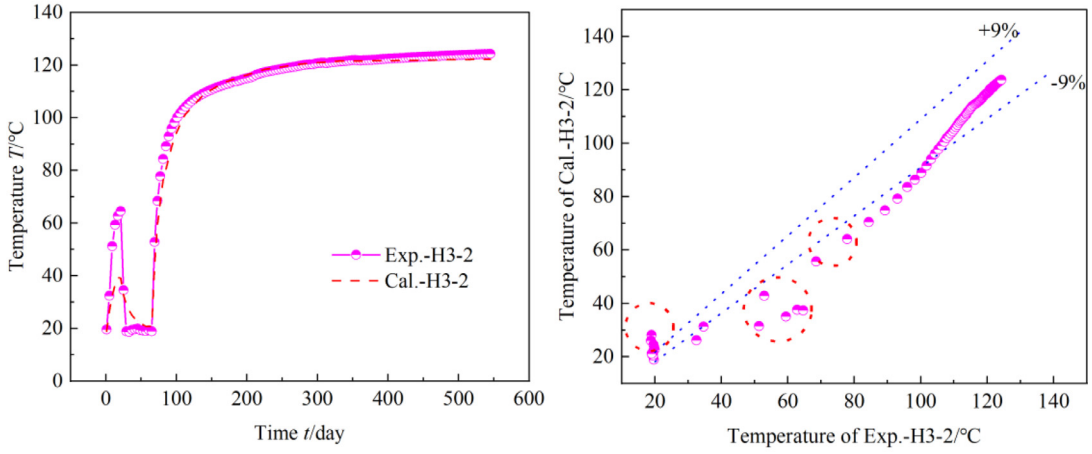

(f) at position of sensor H3-2

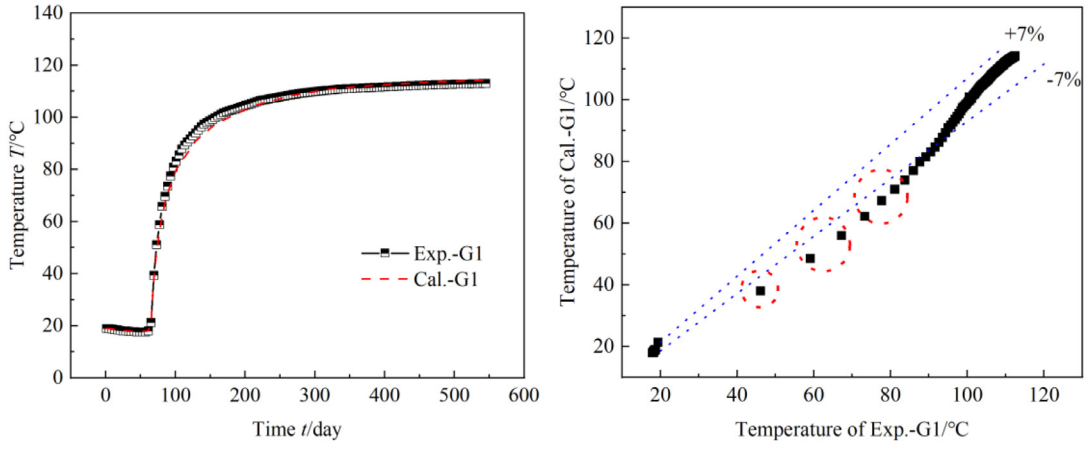

(g) at position of sensor G1

Fig. 11. Continued

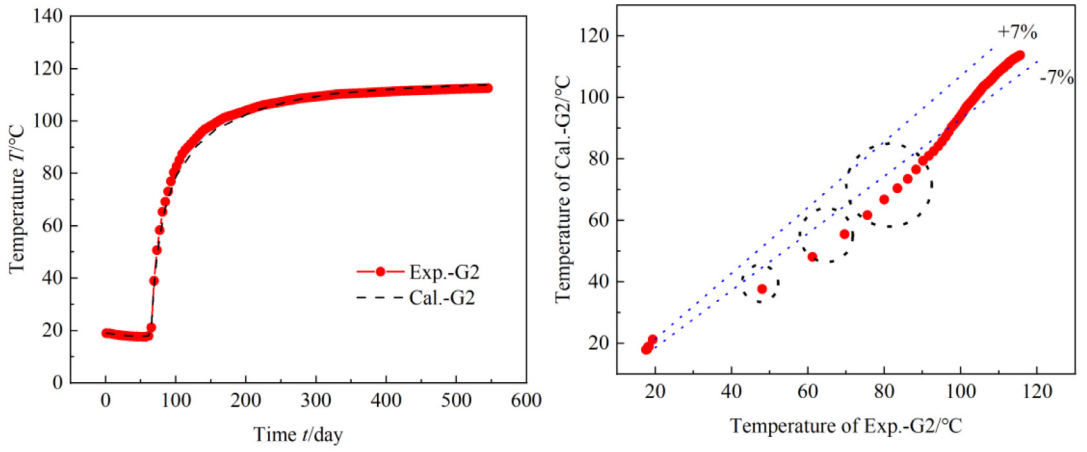

(h) at position of sensor G2

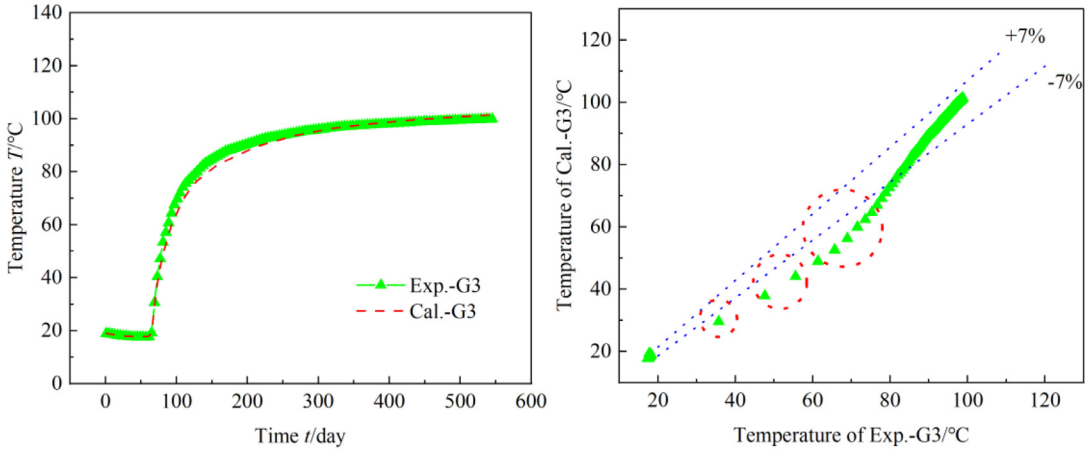

(i) at position of sensor G3

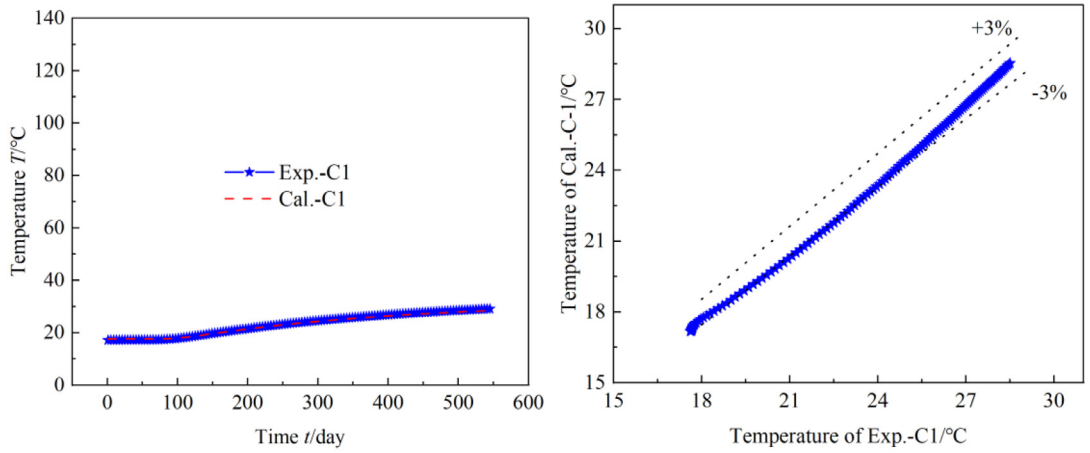

(j) at position of sensor C1

Fig. 11. Continued

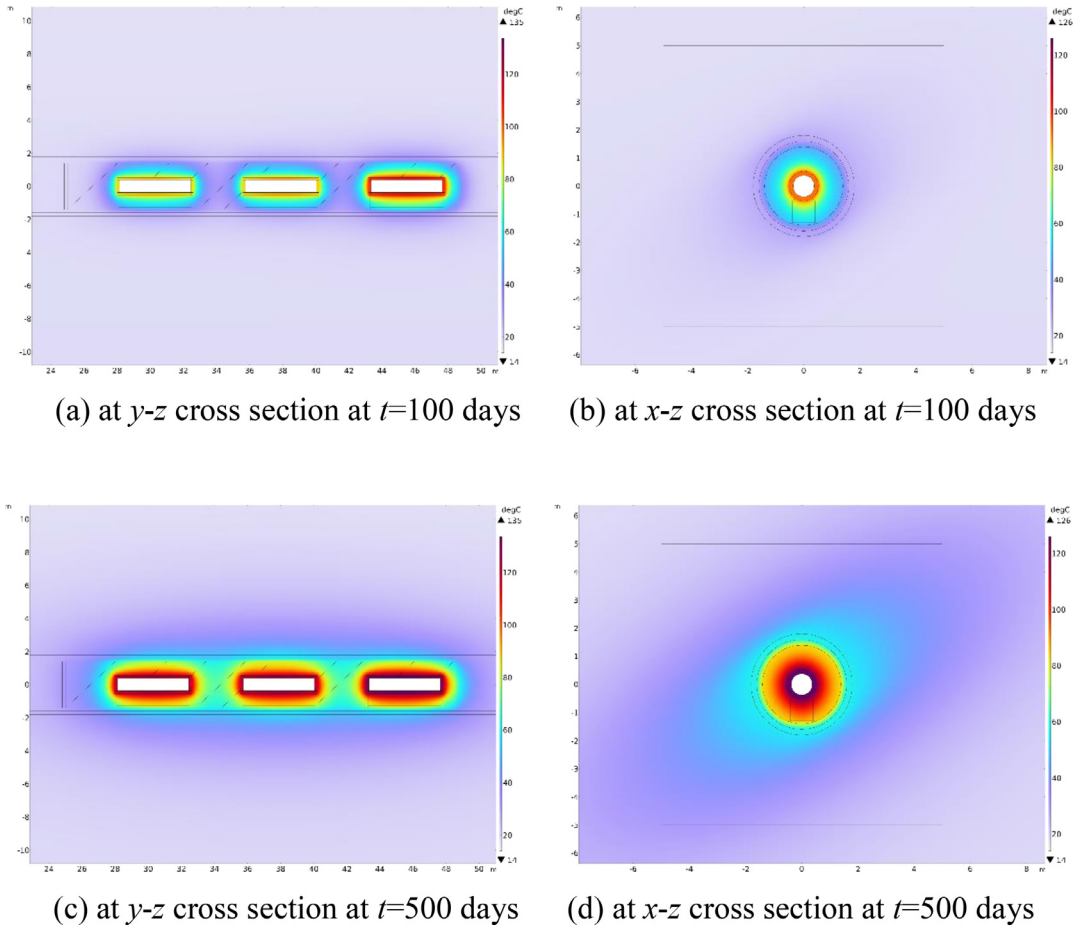

Fig. 12. Temperature distribution of the validation case calculated at *y-z, x-z* cross sections at times t = 100 days and 500 days. (For interpretation of the references to color in this figure legend, the reader is referred to the web version of this article.)

H3–2 and G-2 as shown in Fig. 11, those are quite similar as the other 6 temperature sensors. Therefore, the typical 6 temperature sensors are reasonably selected for the dominant parameters analysis.

In addition to the comparison of temperature evolution at 10 representative sensor locations, the temperature distributions (2D cross section through the 3D model domain) of the validation case at *y-z, x-z* cross sections at the time t = 100 days and 500 days are presented in Fig. 12. According to the boundary condition of the heater 1, specific heat source Q of the heater 1 started earlier than that of other heaters. Hence, the temperature near the heater 1 is larger than that near the other heaters in Fig. 12(a). In Fig. 12(b), the temperature values near heaters are nearly steady state level at the *x-z* cross section. The temperature in the host clay is lower than the near heater GBM region, which is consistent with that in Fig. 11. In Fig. 12(c), the whole tunnel is heated up and the temperature of the clay increased. Especially in Fig. 12(d), the temperature field shows an ellipse pattern with an oblique angle. This reflects the inclination angle of 34° of the bedding plane of the clay with the considered anisotropy of thermal conductivity with higher values parallel to the bedding plane than in the normal direction of the bedding plane.

In total, except the sensor abnormal, the maximum relative errors between the calculation and experimental data are in the reasonable accuracy range of 7%. Discrepancies between the calculation results and experimental data can be attributed to the following reasons. It is assumed that a few humidity sensors represent well the whole 3D saturation degree in the GBM, whereby heterogeneous resaturation is likely to occur, but cannot be measured with enough detail to be used for detailed hydraulic modelling (H modelling of resaturation). Moreover, some sensors operate abnormally during the transient conditions like the heat power sensor data of the heater 3 shown in Fig. 5. It would introduce the additional relative error. This is also confirmed in the reference report [14]. Overall, the calculation results agree well with the large experimental dataset of 137 × 10 data points. Therefore, it illustrates that the ML-assisted heat transport modelling can accurately predict the temperature evolution of the FE experiment.

3.3. Dominant parameters for transient temperature evolution

In order to identify the dominant parameters responsible for the observed temperature evolution in the FE experiment, an orthogonal test method has been used (see Section 2.5). The results are also taken into account for the validation case parameters. At positions of 6 representative sensors H1–1, H2–1, H3–1, G1, G3 and C1, the transient temperature evolution is analysed based on the procedure described in Section 3.2. Particularly, 32 cases are calculated based on the orthogonal test method using parameters values given in Table 5. Variations of the transient temperature evolution for the 3 sensors H1–1, G3 and C1 with parameters are illustrated (Fig. 13). The result for the other 3 sensors H2–1, H3–1 and G1 are added in the Supplementary Material.

For the transient temperature evolution $T_{H1\_1,t}$, $T_{G3,t}$, and $T_{C1,t}$ at time t = 101 days, the response parameters are given in Fig. 13. In addition, a p-test is introduced for the variance analysis. It is the probability that the test statistic can take a value greater than or equal to the value of the test statistic (if the p-value is less than

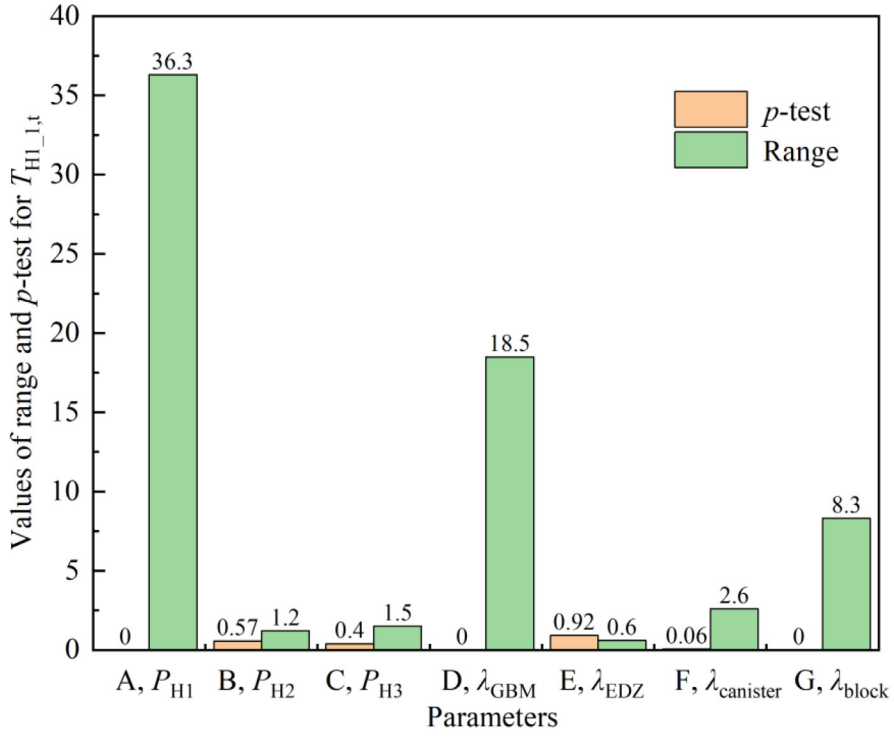

(a) $T_{H1\_1,t}$

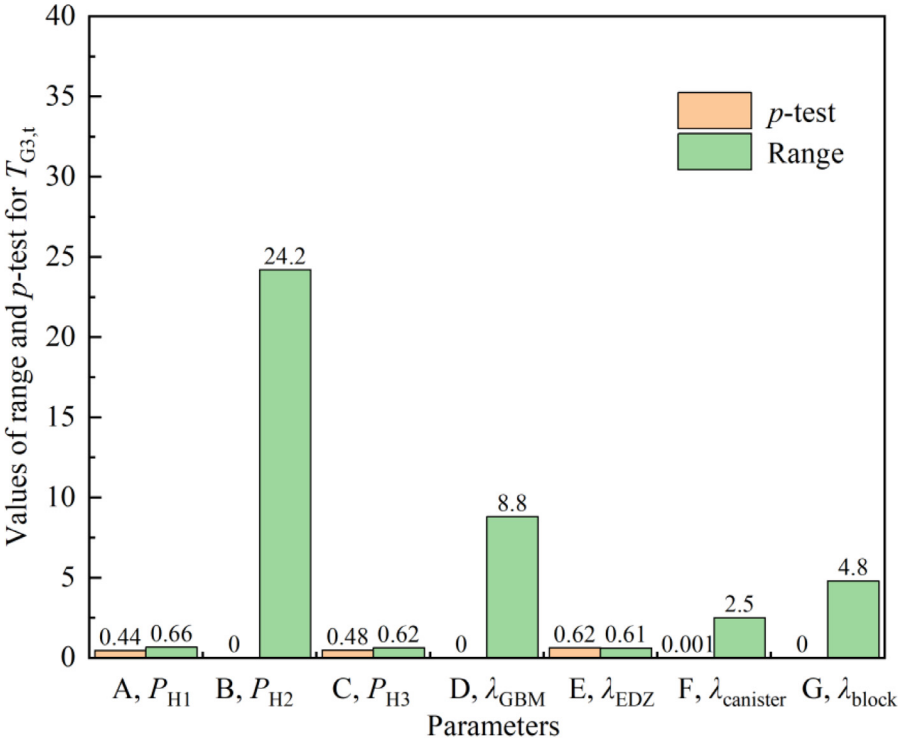

(b) $T_{G3,t}$

Fig. 13. Results of dominant parameters analysis for transient temperature evolution. (For interpretation of the references to color in this figure legend, the reader is referred to the web version of this article.)

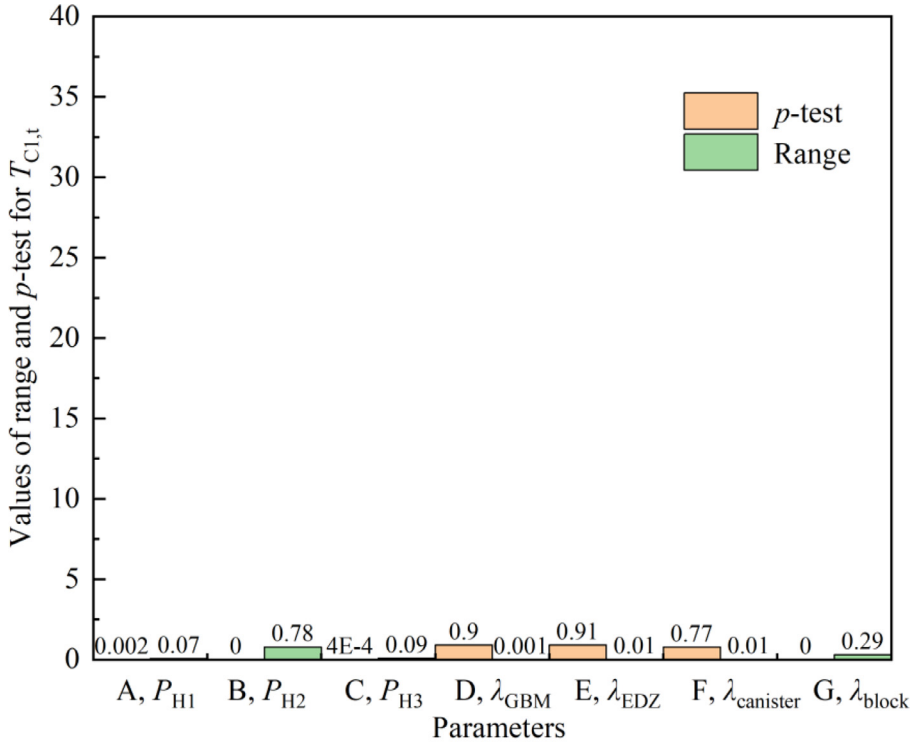

(c) $T_{C1,t}$

Fig. 13. Continued

or equal to the specified significance level 0.1, the null hypothesis is rejected) [49]. A *p*-value less than 0.1 means statistically significant. For example in Fig. 13(a), the *p*-values of 0, 0, 0 and 0.06 reveal that the transient temperature $T_{H1\_1,t}$ is significantly influenced by parameters P_{H1}, λ_{GBM}, λ_{block} and $\lambda_{canister}$ sequentially. In contrast, the *p*-values of 0.92, 0.57 and 0.40 indicate that parameters λ_{EDZ}, P_{H2} and P_{H3} have little effects on the transient temperature $T_{H1\_1,t}$. For the range of each parameter in Fig. 13(a), values of 36.3, 18.5, 8.3 and 2.6 show that the transient temperature $T_{H1\_1,t}$ is also strongly affected by parameters P_{H1}, λ_{GBM}, λ_{block} and $\lambda_{canister}$ sequentially. This is consistent with the variance analysis.

In addition, the transient temperature evolution $T_{G3,t}$ is dominated by parameters P_{H2}, λ_{GBM}, λ_{block} and $\lambda_{canister}$ in order in Fig. 13(b). Transient temperature evolution $T_{C1,t}$ is affected by parameters P_{H2}, λ_{block}, P_{H3}, and P_{H1} sequentially as given in Fig. 13(c). It indicates that the transient temperature far away like the transient temperature evolution $T_{G3,t}$ is more influenced with the corresponding heater power (P_{H1} or P_{H2} or P_{H3}), λ_{GBM}, λ_{block} and $\lambda_{canister}$. However, the transient temperature evolution $T_{C1,t}$ does not change so much compared with that of $T_{H1\_1,t}$ and $T_{G3,t}$. Significant parameters and corresponding mean responses of the transient temperature evolution of $T_{H2\_1,t}$, $T_{H3\_1,t}$, $T_{G2,t}$ are almost quite similar to each other as illustrated in Fig. S2 in Supplementary Material.

Together with the variance and range analysis, the transient temperature evolution near the GBM-heater surfaces and within the GBM mainly rely on the corresponding heat power (P_{H1}, P_{H2} or P_{H3}), and thermal conductivities of the GBM λ_{GBM}, of the bentonite block λ_{block} and of the canister $\lambda_{canister}$ sequentially. In the short term, the transient temperature evolution in the GBM is only affected by the nearest heater power, thermal conductivities of the GBM λ_{GBM}, the bentonite block λ_{block} and the canister $\lambda_{canister}$. Moreover, the transient temperature evolution in the clay is affected by all three heater powers (P_{H1}, P_{H2} and P_{H3}) and thermal conductivity of the bentonite block λ_{block}. It is also due to the fact that the position of the sensor C1 in the clay is relatively close to the bentonite block pedestals. However, the temperature $T_{C1,t}$ changes marginally. This is due to the short heating time period of only 1.5 years and the large distance of C1 to the heaters.

With the help of the dominating parameter analysis, the validation case parameters can be identified. In addition, such an analysis can help to "design" a targeted temperature evolution in the heater near-field. A similar analysis has been performed for the peak temperature of the 6 sensors varying the same parameters, which is presented in Tables S1-S6 in the Supplementary Material.

3.4. Parameter uncertainty and sensor data assessment

Thermal conductivities of the GBM λ_{GBM} and bentonite blocks λ_{block} are functions of the saturation, which strongly affect the simulated temperature evolutions near the heater surface, and in the buffer material and host rock [31].

3.4.1. Parameter uncertainty for FE experiment

Based on [15], bentonite blocks will be stable as long as the ambient air does not exceed the equilibrium relative humidity of the bentonite blocks by more than 5%−10%. Therefore, a subsequent uncertainty range of ±10% is chosen for the thermal conductivity of the bentonite blocks as shown in Table 7. For the concrete material, saturation degree is also quite constant [8]. As there is no specific uncertainty for the thermal conductivity of the concrete material in the FE experiment, a conservative uncertainty range of ±10% is selected. For the saturation degree values, the accuracy of capacitive sensors for the (type Hygrochip HYT-939 and chip SHT75) is ±1.8% [31]. Also, the accuracy of the Elman NN based ML is within ±3.0% (see Section 3.1). Hence, the uncertainty range

Table 7
Parameter uncertainty of three thermal conductivities for FE experiment.

Physical parameters	Minimum value	Maximum value	Reference
Thermal conductivity of GBM λ_{GBM} ($W{\cdot}m^{-1}{\cdot}K^{-1}$)	0.90 × [λ_{GBM1}, .., λ_{GBM10}]	1.10 × [λ_{GBM1}, .., λ_{GBM10}]	[31]
Thermal conductivity of bentonite block λ_{block} ($W{\cdot}m^{-1}{\cdot}K^{-1}$)	0.63	0.77	[15]
Thermal conductivity of concrete $\lambda_{concrete}$ ($W{\cdot}m^{-1}{\cdot}K^{-1}$)	0.18	0.22	[8]

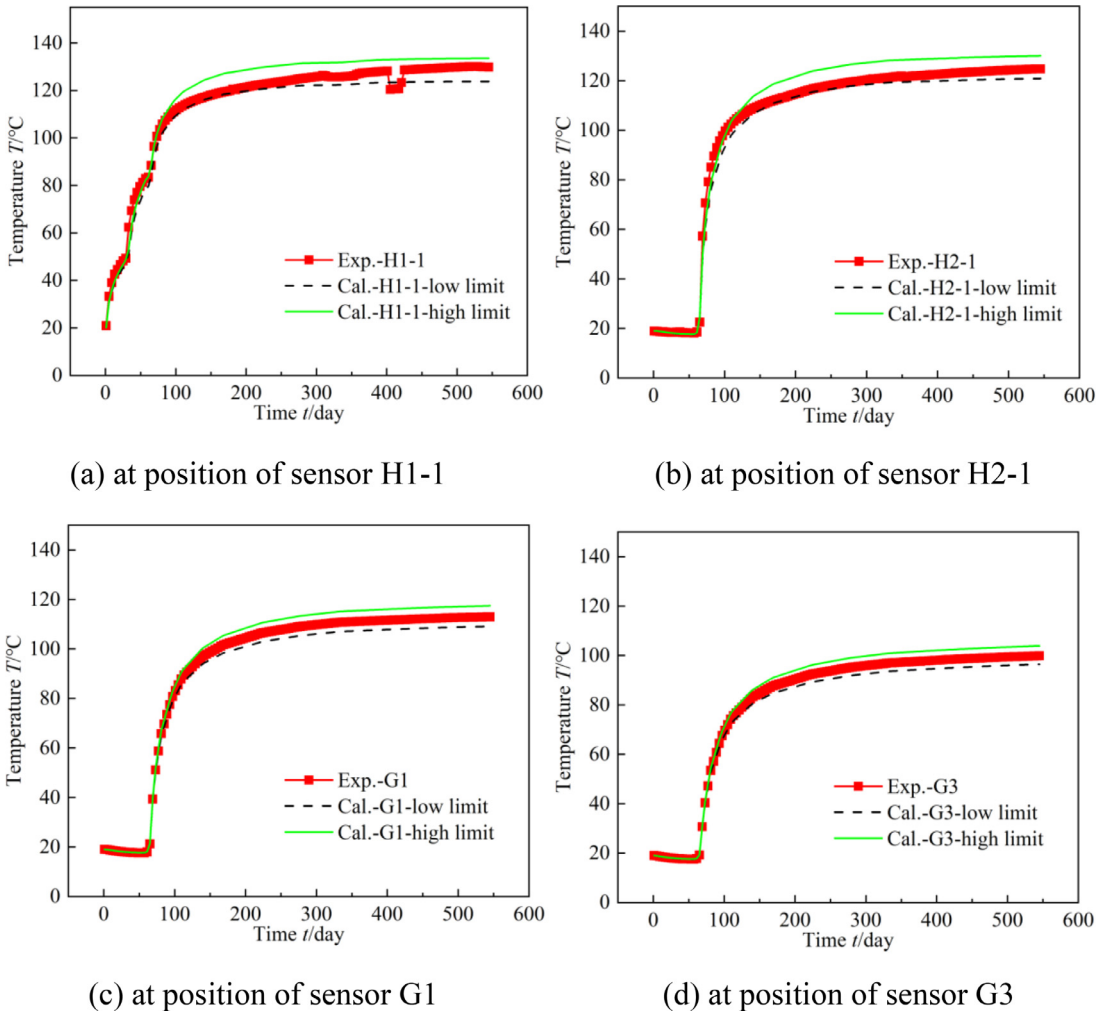

Fig. 14. Bands of temperature uncertainty at positions of sensors H1–1, H2–1, G1, G3 with validation case. (For interpretation of the references to color in this figure legend, the reader is referred to the web version of this article.)

is about ±5.0% for the thermal conductivity of the GBM (from Eq. (7)). Nevertheless, a conservative uncertainty range of ±10% for the thermal conductivity of the GBM λ_{GBM} in Table 7 is chosen to be consistent with that of the thermal conductivity of the bentonite block λ_{block} and concrete $\lambda_{concrete}$. Then, the uncertainty range of ±10% of each parameter is both reasonable and conservative in Table 7. All parameters uncertainties are based on the validation model case described in Section 3.2.

3.4.2. Calculated temperature uncertainty bands and sensor data assessment

Using parameter values given in Table 7, bands of temperature uncertainty are calculated at positions of 6 typical sensors based on the validation case. Calculation results at positions of the sensors H1–1, H2–1, G1, G3 are presented in Fig. 14. The low and high limits are calculated with parameter limits of three thermal conductivities for FE experiment. In addition, the bands of temperature uncertainty at positions of the sensors H3–1, C1 are included in Fig. S5 in Supplementary Material.

From Fig. 14, all the bands of the temperature uncertainty at positions of various sensors are quite narrow during the transient period (t < 150 days) while those are relatively wide after the transient period (t > 150 days). A reason for this behaviour is due to the fact that thermal conductivity of the canister is an order of magnitude larger than that in the GBM, yielding a fast heat transport in the canister and much slower heat transport in the GBM, which causes steep and narrow bands for sensors in the GBM near the canister surface.

As shown in Fig. 14 (also see Fig. S6 in the supplementary material), most of the temperature sensor data are within the band of the calculated temperature uncertainty. However, several experimental data points of the sensor H1–1 are not within such a band of calculated temperature uncertainty for the transient period t > 150 days in Fig. 14(a). A possible explanation is that the

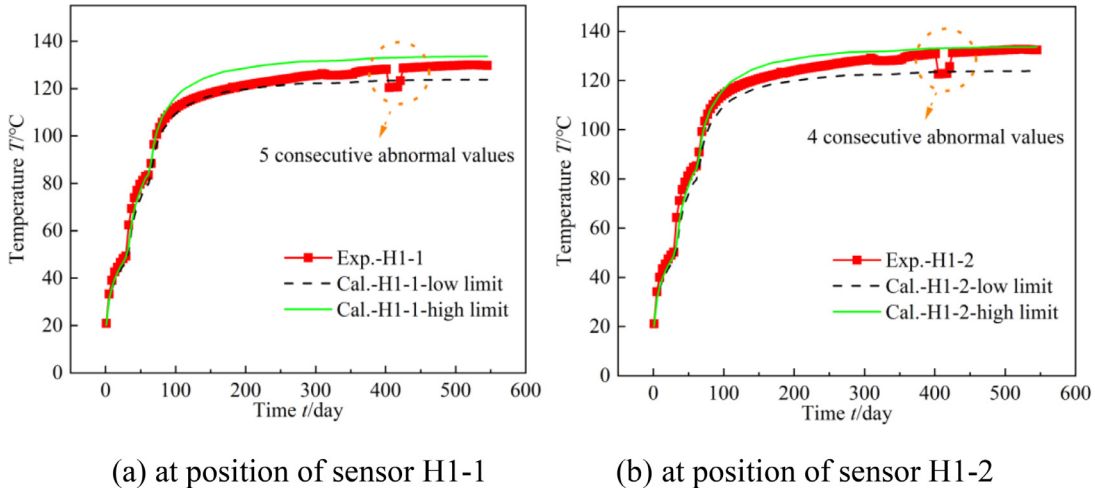

(a) at position of sensor H1-1 (b) at position of sensor H1-2

Fig. 15. Sensor data assessment with temperature T at positions of sensors H1–1, H1–2. (For interpretation of the references to color in this figure legend, the reader is referred to the web version of this article.)

experimental data are abnormal, e.g., outliers, or indicate sensor failure.

A sensor failure detection algorithm (SFDA) is set to be a heuristic criterion, where three or more consecutive faulty data yield a sensor failure [50]. Using the band of calculated temperature uncertainty described before, a method for the sensor data assessment can be proposed as follows: (1) faulty experimental data can be judged by the results of the ML-assisted modelling (bands of temperature uncertainty) taking into account by the influence of parameters uncertainties as described in Section 3.4.2; (2) if more than 3 consecutive experimental data are detected by the SFDA algorithm, i.e. experimental data are outside the band of temperature uncertainty, then these data are identified as faulty data. It should be mentioned that this procedure works better for the smoothly changing temperature sensor data (e.g., after time $t = 137$ days, Fig. 15) than for the strongly increasing temperature data for $t < 137$ days (Fig. 15).

Applying this procedure to temperature data from sensors H1–1 and H1–2 (shown in Fig. 15), results in the detection of 5 and 4 consecutive faulty data at about $t = 410$ days, whereas other sensors nearby don't show faulty data during this time period (see Fig. S6 in the Supplementary Material). This example shows that the developed ML-assisted physically based 3D heat transport model for the FE experiment has been successfully applied to the sensor data assessment, i.e., identify faulty sensor data.

4. Conclusions

A systematical evaluation on the machine learning (ML)-assisted heat transport modelling for the Full-scale Emplacement (FE) experiment at Mont Terri Underground Laboratory (URL) is performed including the data preparation, model validation, identifications of dominant heat transport parameters, investigation of their uncertainties on calculated temperature evolution and application to the sensor data assessment. It includes neural network (NN) based ML methods, physically based surrogate model, COMSOL Multiphysics software, orthogonal test method and range/variance analysis. Main conclusions are:

(1) Data preparation including the normalization and robust NN methods for a raw dataset with a dimensions of 10,960 × 6 is demonstrated. For the ML predicted saturation degree, the Elman NN with a Pearson's r coefficient R of 0.9911, a mean squared error (MSE) of 4.62, and mean absolute error (MAE) of 1.44 operates better than the back propagation (BP) and cascade BP (CBP) NN methods.
(2) Calculation results are compared and validated with a large sensor dataset. During the transient condition, there are few abnormal values due to the sensor failures. Despite these few discrepancies, calculation results agree well with the experimental dataset of 137 × 10 data points with a reasonable error range of 7%.
(3) Each transient temperature evolution and corresponding dominant parameters at positions of 10 typical sensors are obtained from 32 orthogonal test cases. Together with the variance and range analysis, parameters such as the heater power, thermal conductivities of the GBM λ_{GBM}, the bentonite block λ_{block} and the canister $\lambda_{canister}$ have been identified to dominate the temperature evolution at different locations in the near field.
(4) Parameter uncertainty ranges of ±10% for λ_{GBM} and λ_{block} are analysed and bands of temperature uncertainties are compared with temperature sensor data. This allows sensor data assessment including identification of faulty sensor data.
(5) Based on the dominant parameters and parameters uncertainties, a method for the sensor data assessment is proposed. Sensor failures of the sensor H1–1, H1–2 around the time $t = 410$ days are detected with this method.

A ML-assisted physically based 3D heat transport model is developed and successfully applied to the FE experimental conditions. A first step in the direction of a digital twin for the FE experiment is done. Continuously incoming new data will be used to feed the ML-assisted physical modelling framework. Such a framework can be applied to a DGR, help the design, optimization, monitoring setup as well as the assessment of a DGR and provide detailed understandings of the performance behaviour of a DGR.

Declaration of Competing Interest

The authors declare that they have no known competing financial interests or personal relationships that could have appeared to influence the work reported in this paper.

Data availability

Data will be made available on request.

Acknowledgments

This work was partially funded by the European Union's Horizon 2020 research and innovation programme **Eu**ropean Joint Programme on **Rad**ioactive Waste Management in the EURAD MODATS (**Mo**nitoring equipment and **Da**ta **T**reatment for **S**afe repository operation and staged closure) work package [Grant No. 847593]. We express our gratitude and thanks to Dr. Martin Schoenball from Nagra for generously providing the raw data and expressing interest in our research.

Supplementary materials

Supplementary material associated with this article can be found, in the online version, at doi:10.1016/j.ijheatmasstransfer.2023.124290.

References

[1] W. Ricks, J. Norbeck, J. Jenkins, The value of in-reservoir energy storage for flexible dispatch of geothermal power, Appl. Energy (313) (2022) 118807.
[2] G. Chen, L. Tang, B. Mace, et al., Multi-physics coupling in thermoacoustic devices: a review, Renew. Sustain. Energy Rev. (146) (2021) 111170.
[3] C. Esene, S. Zendehboudi, A. Aborig, et al., A modeling strategy to investigate carbonated water injection for EOR and CO2 sequestration, Fuel (252) (2019) 710–721.
[4] H. Xu, J. Ma, P. Tan, et al., Towards online optimisation of solid oxide fuel cell performance: combining deep learning with multi-physics simulation, Energy AI (1) (2020) 100003.
[5] N. Prasianakis, R. Haller, M. Mahrous, et al., Neural network based process coupling and parameter upscaling in reactive transport simulations, Geochim. Cosmochim. Acta (291) (2020) 126–143.
[6] X. Liu, G. Cai, L. Liu, et al., Thermo-hydro-mechanical properties of bentonite-sand-graphite-polypropylene fiber mixtures as buffer materials for a high-level radioactive waste repository, Int. J. Heat Mass Transf. (141) (2019) 981–994.
[7] C. Plúa, M. Vu, G. Armand, J. Rutqvist, et al., A reliable numerical analysis for large-scale modelling of a high-level radioactive waste repository in the Callovo-Oxfordian claystone, Int. J. Rock Mech. Min. Sci. (140) (2021) 104574.
[8] A. Andrés, M. Paul, P. Ivan, et al., FE-Modelling Task Force/Task 1: validation of Thermally Induced THM Effects in the Rock around the FE-Tunnel. NAGRA NAB 19-40, February 2021.
[9] B. Lüthi, FE Experiment: data Trend Report-data from excavation and during 6 years of heating (01.01.2012 –31.08.2021). NAGRA NAB 21-31, April 2022.
[10] B. Bai, T. Xu, Q. Nie, et al., Temperature-driven migration of heavy metal Pb2+ along with moisture movement in unsaturated soils, Int. J. Heat Mass Transf. (153) (2020) 119573.
[11] M. Kim, S. Lee, J. Jeon, et al., Sensitivity analysis of bentonite buffer peak temperature in a high-level waste repository, Ann. Nucl. Energy (123) (2019) 190–199.
[12] M. Villar, G. Armand, N. Conil, et al., Initial State-of-the-Art on THM behaviour of i) Buffer clay materials and of ii) Host clay materials. Deliverable D7.1 HITEC, EURAD Project, Horizon 2020 No. 847593, December 2020.
[13] J. Birkholzer, A. Bond, J. Hudson, et al., DECOVALEX-2015: an international collaboration for advancing the understanding and modeling of coupled thermo-hydro-mechanical-chemical (THMC) processes in geological systems, Environ. Earth Sci. 77 (14) (2018) 1–5.
[14] F. Caporuscio, K. Sauer, M. Rock, et al., Engineered Barrier System R&D and International Collaborations–LANL (FY20): spent Fuel and Waste Disposition. LA-UR-20-25330, July 2020, doi:10.2172/1641554.
[15] Nagra. Implementation of the Full-scale Emplacement Experiment at Mont Terri: design, Construction and Preliminary Results. NAGRA NTB 15-02, May 2019.
[16] G. Hu, W. Pfingsten, Data-driven machine learning for disposal of high-level nuclear waste: a review, Ann. Nucl. Energy (180) (2023) 109452.
[17] G.E. Karniadakis, I.G. Kevrekidis, L. Lu, et al., Physics-informed machine learning, Nat. Rev. Phys. 3 (6) (2021) 422–440.
[18] R.V. Krems, Bayesian machine learning for quantum molecular dynamics, Phys. Chem. Chem. Phys. 21 (25) (2019) 13392–13410.
[19] L. Himanen, A. Geurts, A.S. Foster, et al., Data-driven materials science: status, challenges, and perspectives, Adv. Sci. 6 (21) (2019) 1900808.
[20] B. Ebiwonjumi, A. Cherezov, S. Dzianisau, et al., Machine learning of LWR spent nuclear fuel assembly decay heat measurements, Nucl. Eng. Technol. 53 (11) (2021) 3563–3579.
[21] N. Krishnan, S. Mangalathu, M. Smedskjaer, et al., Predicting the dissolution kinetics of silicate glasses using machine learning, J. Non. Cryst. Solids (487) (2018) 37–45.
[22] J. Birkholzer, C. Tsang, A. Bond, et al., 25 years of DECOVALEX-Scientific advances and lessons learned from an international research collaboration in coupled subsurface processes, Int. J. Rock Mech. Min. Sci. (122) (2019) 103995.
[23] J. Tian, C. Qi, Y. Sun, et al., Permeability prediction of porous media using a combination of computational fluid dynamics and hybrid machine learning methods, Eng. Comput. 37 (4) (2021) 3455–3471.
[24] H.P. Menke, J. Maes, S. Geiger, Upscaling the porosity-permeability relationship of a microporous carbonate for Darcy-scale flow with machine learning, Sci. Rep. 11 (1) (2021) 1–10.
[25] V. Solans, D. Rochman, C. Brazell, et al., Optimisation of used nuclear fuel canister loading using a neural network and genetic algorithm, Neural. Comput. Appl. 33 (23) (2021) 16627–16639.
[26] M. Villar, R. Iglesias, J. García-Siñeriz, State of the in situ Febex test (GTS, Switzerland) after 18 years: a heterogeneous bentonite barrier, Environ. Geotech. 7 (2) (2018) 147–159.
[27] Nagra. The Nagra Research, Development and Demonstration (RD&D) Plan for the Disposal of Radioactive Waste in Switzerland. NAGRA NTB 21-02, November 2021.
[28] H. Müller, B. Garitte, T. Vogt, Implementation of the full-scale emplacement (FE) experiment at the Mont Terri rock laboratory, Swiss J. Geosci. 110 (1) (2017) 287–306, doi:10.1007/s00015-016-0251-2.
[29] T. Sakaki, B. Lüthi, T. Vogt, Investigation of the emplacement dry density of granulated bentonite mixtures using dielectric, mass-balance and actively heated fiber-optic distributed temperature sensing methods, Geomech. Energy Environ. (2022) 100329.
[30] O. Leupin, N. Smart, Z. Zhang, et al., Anaerobic corrosion of carbon steel in bentonite: an evolving interface, Corros. Sci. (187) (2021) 109523.
[31] B. Lanyon, F. Lüthi, E. Manukyan, Interpretation of the First 5 Years of the FE Experiment: a THM Synthesis. NAGRA NAB 19-46, September 2020.
[32] T. Bergman, A. Lavine, F. Incropera, et al., Fundamentals of Heat and Mass Transfer, John Wiley & Sons, 2011 April 12.
[33] C. Lee, J. Lee, S. Park, et al., Numerical analysis of coupled thermo-hydro-mechanical behavior in single-and multi-layer repository concepts for high--level radioactive waste disposal, Tunnel. Undergr. Space Technol. (103) (2020) 103452.
[34] Y. Tan, X. Xu, H. Ming, Analysis of double-layered bu ffer in high-level waste repository, Ann. Nucl. Energy (165) (2022) 108660.
[35] A. Ali, J.M. Bennett, A.A. Biggs, et al., Assessing the hydraulic reduction performance of HYDRUS-1D for application of alkaline irrigation in variably-saturated soils: validation of pH driven hydraulic reduction scaling factors, Agric. Water Manage. (256) (2021) 107101.
[36] P. Xie, T. Li, J. Liu, et al., Urban flow prediction from spatiotemporal data using machine learning: a survey, Aktuel. Aspekte Kernfusionsforsch., Informationstag. 59 (2020) 1–12.
[37] N. Bjorck, C. Gomes, B. Selman, et al., Understanding batch normalization, 32nd Conference on Neural Information Processing Systems, NeurIPS, 2018.
[38] Y. Roh, G. Heo, S. Whang, A survey on data collection for machine learning: a big data-ai integration perspective, IEEE Trans. Knowl. Data Eng. 33 (4) (2019) 1328–1347.
[39] L. Lei, W. Chen, Y. Xue, et al., A comprehensive evaluation method for indoor air quality of buildings based on rough sets and a wavelet neural network, Build. Environ. (162) (2019) 106296.
[40] I. Ozer, O. Cetin, K. Gorur, et al., Improved machine learning performances with transfer learning to predicting need for hospitalization in arboviral infections against the small dataset, Neural. Comput. Appl. 33 (21) (2021) 14975–14989.
[41] H. Ansari, M. Zarei, S. Sabbaghi, et al., A new comprehensive model for relative viscosity of various nanofluids using feed-forward back-propagation MLP neural networks, Int. Commun. Heat Mass Transf. (91) (2018) 158–164.
[42] Y. Chen, Z. He, Z. Shang, et al., A novel combined model based on echo state network for multi-step ahead wind speed forecasting: a case study of NREL, Energy Convers. Manage. (179) (2019) 13–29.
[43] D. Jia, Z. Wu, Seismic fragility analysis of RC frame-shear wall structure under multidimensional performance limit state based on ensemble neural network, Eng. Struct. (246) (2021) 112975.
[44] L. Tang, S. Na, Comparison of machine learning methods for ground settlement prediction with different tunneling datasets, J. Rock Mech. Geotech. Eng. 13 (6) (2021) 1274–1289.
[45] G. Zhang, G. Tian, D. Cai, et al., Merging radar and rain gauge data by using spatial-temporal local weighted linear regression kriging for quantitative precipitation estimation, J. Hydrol. (Amst.) (601) (2021) 126612.
[46] H. Bang, S. Yoon, H. Jeon, Application of machine learning methods to predict a thermal conductivity model for compacted bentonite, Ann. Nucl. Energy (142) (2020) 107395.
[47] A. Papafotiou, R. Senger, C. Li, et al., A prediction-evaluation approach to the full-scale emplacement experiment (FE) in Mont Terri, Geol. Soc., Lond., Spec. Publ. 482 (1) (2019) 39–73.
[48] B. Garitte, H. Müller, T. Vogt, et al., Scoping computations for the full-scale emplacement (FE) experiment at the Mont Terri underground research laboratory, International Conference on the Performance of Engineered Barriers, February 6-7, 2014.
[49] G. Hu, H. Zhang, Q. Liu, Design optimization on characteristics of packed-bed thermal energy storage system coupled with high temperature gas-cooled reactor pebble-bed module, Energy Convers. Manage. (257) (2022) 115434.
[50] K. Thiyagarajan, S. Kodagoda, L. Van Nguyen, et al., Sensor failure detection and faulty data accommodation approach for instrumented wastewater infrastructures, IEEE Access (6) (2018) 56562–56574.